Int. J. Nonlinear Anal. Appl. In Press, 1–30
ISSN: 2008-6822 (electronic)
http://dx.doi.org/10.22075/ijnaa.2024.29370.4138

Sliding mode leader-follower formation protocol design for nonlinear model of multi quadrotor

Reza Ghasemi[a,*], Fatemeh Ghaderi[b], Alireza Toloei[b,*]

[a]Department of Electrical Engineering, University of Qom, Qom, Iran
[b]Department of Aerospace Engineering, Shahid Beheshti University, Tehran, Iran

(Communicated by Haydar Akca)

Abstract

This paper deals with designing a sliding mode formation controller for a group of quadrotors in the presence of disturbances and uncertainties. In this approach, first-order, terminal, super-twisting, and nonsingular super-twisting terminal sliding mode controllers were developed and compared with each other. In the first-order controller, the phenomenon of chattering was observed in the control commands, which was solved by using the boundary layer method. Also, the results of the sensitivity analysis of the controllers showed that the nonsingular super-twisting terminal controller is less sensitive to the variation of the controller parameters, so this method was applied to control both the position and attitude of the flight formation of quadrotors. The formation strategy is based on a leader-follower approach. The leader tracks the prescribed reference trajectory, and the followers retain a constant distance from the leader. In addition, the proposed controllers are applied in the form of three missions to validate the formation controller results. In the first mission, the formation of three triangular quadrotors along the spiral path has been successfully attained. In the second task, the three quadrotors linearly track the S-shaped path. The third one is the same as the previous one, except that the number of quadrotors has increased to five. The results of the simulation showed that the convergence time and the overshoot/undershoot of the outputs are less than the other three methods in the nonsingular super-twisting terminal sliding mode controller. The simulation results for the mentioned missions for different paths, geometries, and the number of quadrotors indicate that the applied method has been successful in reducing the effects of disturbances and uncertainties, and the agents succeed in formation flight precisely.

Keywords: Formation Control, Leader-Follower Formation, Quadrotor, Sliding Mode Control, Terminal Super-Twisting
2020 MSC: 34Hxx

1 Introduction

Recently, the use of quadrupoles for various applications has increased. Due to the non-linear dynamics of this aircraft, different control methods are used, the most important of which is the sliding mode controller. For example, in [8], an adaptive non-singular sliding mode controller is applied to control the attitude and altitude of the quadrotor with three degrees of freedom, concerning limited disturbances. In [13], a non-singular terminal sliding surface based

*Corresponding author
Email addresses: r.ghasemi@qom.ac.ir (Reza Ghasemi), ghaderi70@sbu.ac.ir (Fatemeh Ghaderi), toloei@sbu.ac.ir (Alireza Toloei)

Received: January 2023 *Accepted:* September 2024

on a sliding mode controller is proposed for the tracking problem of a quadrotor in the presence of external disturbances. The PID sliding surface is designed to eliminate the steady-state error and improve the robustness of attitude and position subsystems. In reference [17], the problem of robust attitude control for a quadrotor operating in an environment polluted with lumped disturbances is considered. A new continuous terminal sliding mode based on active anti-disturbance control (CTSMBAADC) is proposed by innovatively introducing a finite time disturbance observer (FTDO) in homogeneous continuous nonsingular terminal sliding mode. [14] investigates the terminal sliding-mode control (TSMC) with predefined time stability (PTS) for a disturbed quadrotor system (DQS). First, for both the rotational and translational subsystems of the DQS, a novel notion of predefined-time terminal sliding-mode manifold (PTTSMM) is created. Using the proposed PTTSMM method, the DQS state variables reach their origin in a predefined time. In [26], addressing such problems as the chattering phenomenon and slow speed of keeping up with the predetermined trajectory in the application of sliding mode control to a quadrotor, a rare nonlinear sliding mode control strategy is proposed. [18] solves an accurate fixed-time attitude and position control problem of a quadrotor UAV system. Robust nonlinear control strategies for attitude and position control are innovatively proposed based on a new continuous nonsingular terminal sliding mode control (CNTSMC) scheme. A full-order homogeneous terminal sliding surface is designed for the attitude and position states in such a way that the sliding motion is fixed-time stable independently of the system's initial condition. Hence, this contributes to enhancing the control system's robustness. In [10], a novel flight controller is proposed based on the chattering-reduced terminal sliding mode control method and a universal nonlinear disturbance estimator (NDE), which is applied to improve the robustness of the flight system. By skillfully using Lyapunov theory, the stability condition of the closed-loop systems is derived, and it is shown that the control gains can be reduced by estimating the model uncertainties and external disturbances.

Over the past decade, the multiple quadrotor formation procedure has obtained extensive attention in changing climates and complex environments. Formation Flight provides the solicitation of groups in various applications, such as inaccessible area recognition, disaster management, search in hard-to-reach areas, etc [11]. The mentioned programs require more than one quadrotor to achieve the intended purpose. Numerous controller methodologies have been developed to solve the formation flight problem. One of the most important techniques is the leader-follower strategies that derive from [15]. Distributed and decentralized procedures are the two main approaches for leader-follower policies. In distributed control, part of the followers receive the leader's information, but there are interactions between the followers [7]. On the other hand decentralized mechanism, followers can receive the leader's information [5]. In [6], the distributed leader-follower problems have been analyzed by a set of rigid-body spacecraft based on the representation of the quaternary. A Linear Quadratic Regulator (LQR) for individual and group quadrotor flight is also proposed in [1]. The simulation results showed the controller's ability to overcome communication topology changes between quadrotors. In [20], the optimal methodology is considered to reach the formation. Neuro-controller was derived to reach leader-follower in [21] with guaranteed Lyapunov stability. Using graph theory, a backstepping controller was developed to touch the distance-based formation for group robots in [3]. A coordinated group flight control is designated to alleviate the time delay in communication in [22].

Authors in [16] present a 3-D motion distributed controller scheme to conserve the distance-based formation of multi-agents. In [12], model predictive techniques have been applied to reach obstacle-avoidance flight formation. The model predictive controllers have been introduced for the formation control of drones in [23], and the simulations and experimental results showed the capability of the procedure to steer drones in the desired radius. Flight formation is developed for both collision and obstacle avoidance in [24]. In [25], the authors propose feedback formation controllers to track the prescribed path. Then they proposed a nonlinear decentralized formation controller for the problem of aggressive group flight of quadrotors in [4], where the communication effect is considered in the performance of the flight group.

The authors in [15] then proposed both the decentralized D-CAPT and the centralized C-CAPT to solve the simultaneous operation for the quadrotor group flight, and the comparison of the mentioned methods was done both experimentally and theoretically in the presence of external disturbances. [2] proposes a fast terminal sliding mode control (SMC) method for the formation of heterogeneous multi-agent systems (MASs) with a fixed topology using a virtual leader. [19] presents a formation tracking control method for the operation of multi-agent systems under disturbances. This study aims to ensure that the followers of a quadcopter converge into the desired formation while the center formation of the follower quadcopters tracks the leader's trajectory within a finite time. The distributed finite-time formation control problem is first investigated using the fast terminal sliding mode control (FTSMC) theory. A disturbance observer is then integrated into the FTSMC to overcome the model uncertainties and bounded disturbances.[9] proposes a dynamic model based on distance and orientation between an omnidirectional mobile robot and a quadrotor Unmanned Aerial Vehicle (UAV), both under the leader–follower scheme. It is assumed that the omnidirectional robot is already controlled to follow the desired trajectory.

In the previous paper, the comparison between different sliding mode controller methods and the superiority of the methods have not been discussed. Also, a few past works have dealt with chattering removal with the boundary layer method. The sensitivity analysis of the parameters has also received less attention. Also, in the discussion of formation articles, the control of position and situation with the non-singular terminal super twisting sliding mode method has been discussed in a few works.

In this paper, the nonlinear dynamical model of the quadrotor is considered in the presence of disturbances and uncertainties. The first-order, nonsingular terminal, super-twisting, and nonsingular terminal super-twisting sliding mode controllers were applied to control the position and attitude of the quadrotor. Based on the simulation results, the finite time convergence of the tracking error to zero, and decreasing in the chattering phenomena are the main merits of the super-twisting nonsingular terminal SMCs for flight formation. Finally, the proposed formation controllers are validated in the form of three missions. The organization of the present article is explained as follows: a quadrotor dynamic model is provided in Section 2. The first-order SMC is presented in Section 3. The design of nonsingular terminal SMC is proposed in Section 4. Section 5 depicts super-twisting SMC. Section 6 illustrates a nonsingular terminal super twisting SMC. Section 7 is dedicated to illustrating formation control. Eventually, a brief summarization is presented in the last section.

2 Quadrotor Dynamic Model

The quadrotor consists of a rigid body equipped with four rotors (Figure 1). The two pairs of rotors (1,3) and (2,4) turn in the opposite direction to balance or produce the yaw motion. The 6-DOF dynamic model of quadrotors, as well as the model of actuators, is presented in this section. Modelling assumptions include the following:

The body is considered rigid and symmetrical. The lifts and reactive moment produced by four rotors, respectively, are proportional to the square of their rotational speed. The dynamical model of the quadrotor can be obtained in two ways: Newton-Euler and Euler-Lagrange. Here, the quadrotor model is obtained according to the Newton-Euler method in [**?**]. Equation 2.1 shows the general kinematics of a rigid body with six degrees of freedom:

$$\dot{\xi} = J_\theta \nu \tag{2.1}$$

$\dot{\xi}$ is the general velocity vector in inertial coordinates, ν is the general velocity vector in body coordinates, and J_θ is the generalized matrix. ξ is a combination of linear position vectors Γ^E and angular Θ^E of the quadrotor in inertial coordinates, which is shown by equation 2.2:

$$\xi = \begin{bmatrix}\Gamma^E & \Theta^E\end{bmatrix}^T = \begin{bmatrix}X & Y & Z & \phi & \theta & \Psi\end{bmatrix}^T \tag{2.2}$$

Similarly, ν is a combination of linear velocity V^B and angular velocity ω^B of the quadrotor in body coordinates and is shown by equation :

$$\nu = \begin{bmatrix}V^B & \omega^B\end{bmatrix}^T = \begin{bmatrix}u & \vartheta & w & p & q & r\end{bmatrix}^T \tag{2.3}$$

In addition, the generalized matrix J_θ consists of four submatrices according to equation 2.4:

$$J_\theta = \begin{bmatrix} R_\Theta & 0_{3\times3} \\ 0_{3\times3} & T_\Theta \end{bmatrix} \tag{2.4}$$

where $0_{3\times3}$ is a submatrix with dimensions 3×3, so that all its rows are zero. The rotation matrix R_Θ and the transfer matrix T_Θ are the matrices defined according to equations 2.5 and 2.6.

$$R_\Theta = \begin{bmatrix} C_\Psi C_\theta & C_\Psi S_\theta S_\phi - S_\Psi C_\phi & C_\Psi S_\theta C_\phi + S_\Psi S_\phi \\ S_\Psi C_\theta & S_\Psi S_\theta S_\phi - C_\Psi C_\phi & S_\Psi S_\theta S_\phi - C_\Psi S_\phi \\ -S_\theta & C_\theta S_\phi & C_\theta C_\phi \end{bmatrix} \tag{2.5}$$

$$T_\Theta = \begin{bmatrix} 1 & S_\phi t_\theta & C_\phi t_\theta \\ 0 & C_\phi & -S_\phi \\ 0 & \frac{-S_\phi}{C_\theta} & \frac{C_\phi}{C_\theta} \end{bmatrix} \tag{2.6}$$

where $C_k = \cos k, S_k = \sin k, t_k = \tan k$. The general dynamics of a 6-degree-of-freedom object are as follows:

$$\begin{bmatrix} mI_{3\times3} & 0_{3\times3} \\ 0_{3\times3} & I \end{bmatrix} \begin{bmatrix} \dot{V}^B \\ \dot{\omega}^B \end{bmatrix} + \begin{bmatrix} \omega^B \times (mV^B) \\ \omega^B \times (I\omega^B) \end{bmatrix} = \begin{bmatrix} F^B \\ \tau^B \end{bmatrix} \tag{2.7}$$

where m is the mass of the body and I is the inertial matrix. V^B is the linear acceleration vector of the quadrotor and ω^B is the angular acceleration vector of the quadrotor in body coordinates. In addition, F^B is the quadrotor force vector, and τ^B is the quadrotor torque vector in body coordinates. The total force vector can be defined as follows:

$$\Lambda = \begin{bmatrix} F^B & \tau^B \end{bmatrix}^T = \begin{bmatrix} F_x & F_y & F_z & \tau_x & \tau_y & \tau_z \end{bmatrix}^T \tag{2.8}$$

Therefore, equations 2.1, 2.2, ..., 2.7 can be rewritten in the matrix form below:

$$M_B \dot{\nu} + C_B(\nu)\nu = \Lambda \tag{2.9}$$

$\dot{\nu}$ is the total acceleration vector in body coordinates. M_B is the inertia matrix of the system in body coordinates and C_B is the Coriolis matrix in body coordinates. The following equation shows the inertia matrix of the system.

$$M_B = \begin{bmatrix} mI_{3\times3} & 0_{3\times3} \\ 0_{3\times3} & I \end{bmatrix} = \begin{bmatrix} m & 0 & 0 & 0 & 0 & 0 \\ 0 & m & 0 & 0 & 0 & 0 \\ 0 & 0 & m & 0 & 0 & 0 \\ 0 & 0 & 0 & I_{xx} & 0 & 0 \\ 0 & 0 & 0 & 0 & I_{yy} & 0 \\ 0 & 0 & 0 & 0 & 0 & I_{zz} \end{bmatrix} \tag{2.10}$$

The Coriolis matrix is also given below.

$$C_B(\nu) = \begin{bmatrix} 0_{3\times3} & -mS(V^B) \\ 0_{3\times3} & -S(I\omega^B) \end{bmatrix} = \begin{bmatrix} 0 & 0 & 0 & 0 & mw & -mv \\ 0 & 0 & 0 & -mw & 0 & mu \\ 0 & 0 & 0 & mv & -mu & 0 \\ 0 & 0 & 0 & 0 & I_{zz}r & I_{yy}q \\ 0 & 0 & 0 & -I_{zz}r & 0 & I_{xx}p \\ 0 & 0 & 0 & I_{yy}q & -I_{xx}p & 0 \end{bmatrix} \tag{2.11}$$

where S is the symmetry deviation. For a three-dimensional vector k, the symmetry deviation matrix is as follows.

$$S(k) = -S^T(k) = \begin{bmatrix} 0 & -k_3 & k_1 \\ k_3 & 0 & -k_1 \\ -k_2 & k_1 & 0 \end{bmatrix}, \quad k = \begin{bmatrix} k_1 \\ k_2 \\ k_3 \end{bmatrix} \tag{2.12}$$

The following equation introduces the total rotors velocity and its vector:

$$\Omega = -\Omega_1 + \Omega_2 - \Omega_3 + \Omega_4, \quad \Omega = \begin{bmatrix} \Omega_1 \\ \Omega_2 \\ \Omega_3 \\ \Omega_4 \end{bmatrix} \tag{2.13}$$

where Ω_1, Ω_2, Ω_3, and Ω_4 are the velocity of the front, right, rear, and left rotor. The following equation shows the effect of the motion vector on the quadrotor dynamics.

$$U_B(\Omega) = E_B\Omega^2 = \begin{bmatrix} 0 \\ 0 \\ U_1 \\ U_2 \\ U_3 \\ U_4 \end{bmatrix} = \begin{bmatrix} 0 \\ 0 \\ b(\Omega_1^2 + \Omega_2^2 + \Omega_3^2 + \Omega_4^2) \\ bl(\Omega_4^2 - \Omega_2^2) \\ bl(\Omega_3^2 - \Omega_1^2) \\ c_d(\Omega_2^2 + \Omega_4^2 - \Omega_1^2 - \Omega_3^2) \end{bmatrix} \tag{2.14}$$

where l is the length from the center of mass to each rotor, c_T depicts the thrust force coefficient, c_d illustrates the drag force coefficient, E_B represents the motion matrix, and $U_B(\Omega)$ is the motion vector.

$$E_B = \begin{bmatrix} 0 & 0 & 0 & 0 \\ 0 & 0 & 0 & 0 \\ c_T & c_T & c_T & c_T \\ 0 & -c_T l & 0 & c_T l \\ -c_T l & 0 & c_T l & 0 \\ -c_d & c_d & -c_d & c_d \end{bmatrix} \tag{2.15}$$

According to equation 9, the dynamics of the quadrotor can be written as follows:

$$M_B\dot{\nu} + C_B(\nu)\nu = G_B(\xi) + O_B(\nu)\Omega + E_B\Omega^2 \tag{2.16}$$

where $G_B(\xi)$ is the gravity vector and $O_B(\nu)$ is the gyroscopic matrix of the rotor, which is defined as follows:

$$O_B(\nu)\Omega = \begin{bmatrix} 0_{3\times3} \\ -\sum_{k=1}^{4} J_{TP}\left(\omega^B \times \begin{bmatrix}0\\0\\1\end{bmatrix}\right)(-1)^k\Omega_k \end{bmatrix} = \begin{bmatrix} 0_{3\times1} \\ J_{TP}\begin{bmatrix}-q\\p\\r\end{bmatrix}\Omega \end{bmatrix} = J_{TP}\begin{bmatrix} 0 & 0 & 0 & 0 \\ 0 & 0 & 0 & 0 \\ 0 & 0 & 0 & 0 \\ q & -q & q & -q \\ -p & p & -p & p \\ 0 & 0 & 0 & 0 \end{bmatrix}\Omega$$

J_{Tp} is the moment of total rotation of inertia about the rotor axis. Eventually, the dynamical model of the quadrotor is as follows:

$$\dot{U} = (RV - QW) + g\sin\theta \tag{2.17}$$

$$\dot{V} = (PW - RU) - g\cos\theta\sin\phi \tag{2.18}$$

$$\dot{W} = (PV - QU) - g\cos\theta\sin\phi + \frac{U_1}{m} \tag{2.19}$$

$$\dot{P} = \frac{I_{yy} - I_{zz}}{I_{xx}}RQ - \frac{J_{Tp}}{I_{xx}}Q\Omega + \frac{U_2}{I_{xx}} \tag{2.20}$$

$$\dot{Q} = \frac{I_{zz} - I_{xx}}{I_{yy}}RP + \frac{J_{Tp}}{I_{yy}}P\Omega + \frac{U_3}{I_{yy}} \tag{2.21}$$

$$\dot{R} = \frac{I_{xx} - I_{yy}}{I_{zz}}PQ + \frac{U_4}{I_{zz}} \tag{2.22}$$

where (U, V, W) shows the speed vector, (P, Q, R) illustrate the roll, pitch, and yaw angles, I_{xx}, I_{yy}, and I_{zz} are the moments of inertia about the x, y, and z-axis, whose all values are given in Table 1. Correspondingly, the U_1, U_2, U_3, and U_4 as the rotor's speed are obtained from the following equations:

$$U_1 = c_T(\Omega_1^2 + \Omega_2^2 + \Omega_3^2 + \Omega_4^2) \tag{2.23}$$

$$U_2 = lc_T(-\Omega_2^2 + \Omega_4^2) \tag{2.24}$$

$$U_3 = lc_T(-\Omega_1^2 + \Omega_3^2) \tag{2.25}$$

$$U_4 = c_d(-\Omega_1^2 + \Omega_2^2 - \Omega_3^2 + \Omega_4^2) \tag{2.26}$$

$$\Omega = -\Omega_1 + \Omega_2 - \Omega_3 + \Omega_4 \tag{2.27}$$

Table 1: Quadrotor model parameters used in the simulation

Value	Parameters
$11 \times 10^{-2}\ kg\ m^2$	I_{xx}
$19 \times 10^{-2}\ kg\ m^2$	I_{yy}
$1.3 \times 10^{-2}\ kg\ m^2$	I_{zz}
$6 \times 10^{-5}\ kg\ m^2$	J_{Tp}
$3.23\ kg$	m
$0.23\ m$	l
$7.5 \times 10^{-7}\ N\ m\ s^2$	c_d
$3.13 \times 10^{-5}\ N\ s^2$	c_T

2.1 Actuators Dynamic Model

Considering that the dynamics of the actuator are not the main focus of this research, we describe the dynamics of each actuator approximately by the following first-order inertial element:

$$\frac{\omega(s)}{\omega_r(s)} = \frac{1}{T_{act}s + 1} \tag{2.28}$$

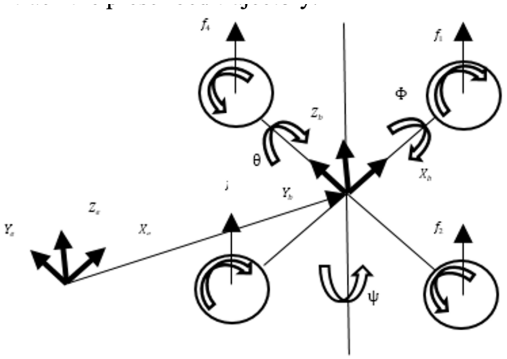

Figure 1: Quadrotor scheme

where T_{act} is the time constant of the actuator dynamics, ω_r and ω are desired rotation speed and actual rotation speed of the actuator. We assume that max $0 \leq \omega_r \leq \omega_{\max}$, where $\omega_{\max}$ is the maximum rotation speed of the practical electric motor. considering the different time scales, the control laws of the actuator servo system and the quadrotor system are designed separately. Thus, we neglect the controller for the actuator system in this paper and such first-order inertia element assumption is reasonable.

3 Sliding Mode Controller

The sliding mode control approach is recognized as one of the efficient tools to design robust controllers for complex high-order nonlinear dynamic plants operating under uncertain conditions. The major advantage of sliding mode is low sensitivity to plant parameter variations and disturbances which eliminates the necessity of exact modeling. Sliding mode control enables the decoupling of the overall system motion into independent partial components of lower dimensions and, as a result, reduces the complexity of feedback design. Sliding mode control implies that control actions are discontinuous state functions that may easily be implemented by conventional power converters with "on-off" as the only admissible operation mode. In the following, the design of four sliding mode control methods has been discussed.

3.1 First-Order SMC

The nonlinear system is considered in the following form:

$$x^{(n)}(t) = f(x.t) + g(x.t)u(t) + d(t) \tag{3.1}$$

where $d(t)$ includes parametric uncertainties, unmodeled dynamics, and disturbance.

$$d(t) \leq D \tag{3.2}$$

where D is the maximum disturbance and is a positive number. In this paper, the wind disturbance was considered as follows;

$$V_x = 0.5 \sin(0.1\ t - \pi) \tag{3.3}$$
$$V_y = 0.5 \sin(0.1\ t - \pi). \tag{3.4}$$

To design a classic SMC, it is first necessary to define the sliding surface as follows [15]:

$$S = \left(\frac{d}{dt} + \lambda\right)^{n-1} \widetilde{x} \tag{3.5}$$

where,

$$\widetilde{x} = x - x_d = e. \tag{3.6}$$

The sliding surfaces for the quadrotor are considered as follows:

$$S_\varphi = \dot{\widetilde{\varphi}} + \lambda\widetilde{\varphi} \tag{3.7}$$

$$S_\theta = \dot{\widetilde{\theta}} + \lambda\widetilde{\varphi} \tag{3.8}$$

$$S_\psi = \dot{\widetilde{\psi}} + \lambda\widetilde{\psi} \tag{3.9}$$

$$S_x = \dot{\widetilde{x}} + \lambda\widetilde{x} \tag{3.10}$$

$$S_y = \dot{\widetilde{y}} + \lambda\widetilde{y} \tag{3.11}$$

$$S_z = \dot{\widetilde{z}} + \lambda\widetilde{z}. \tag{3.12}$$

The Lyapunov stability of the sliding surface will ensure the stability of the system states; Therefore, considering the appropriate Lyapunov function as below and examining its changes, a control law will be designed to achieve asymptotic stability.

$$V = \frac{1}{2}s^2 \tag{3.13}$$

$$\dot{V} = s\dot{s}. \tag{3.14}$$

As a result, the sliding surface s will converge to zero only if:

$$s\dot{s} < 0. \tag{3.15}$$

The above equation shows a condition on the sliding variable s and its first derivative and it is a condition of reaching. If s satisfies any of the following equations, so that k_1 and k_2 are positive constants, then s satisfies the condition of reaching.

$$\dot{s} = -k_1 s - k_2 sgn(s). \tag{3.16}$$

The sliding mode controller consists of two parts: equivalent control and discontinuous control:

$$U_n = u_{eqn} + u_{disn}, \quad n = 1, 2, 3, x, y, z \tag{3.17}$$

that u_{eq} is obtained by setting the sliding surface derivative equal to zero and u_{dis} is obtained by satisfying the Lyapunov stability condition of the sliding surface. By putting $\dot{s}$ in the form of the above functions, discontinuous control can be considered as one of the following functions:

$$u_{disc} = -k_1 s - k_2 sgn(s) \tag{3.18}$$

Using equation (3.1), equation (3.15) can be rewritten as below.

$$\dot{V} = s\dot{s} \leq -\eta \tag{3.19}$$

$$s\dot{s} \leq -\eta|s| \tag{3.20}$$

$$s\left(f(x) + g(x)u + d(t)\right) \leq -\eta|s|. \tag{3.21}$$

By substituting equations (3.16) and (3.17), we have:

$$s\left(-k_2 sgn(s) + d(t)\right) \leq -k_2|s| + |s|\,|d(t)| \tag{3.22}$$

$$|s|(-k_2 + |d(t)|) \leq -\eta|s|. \tag{3.23}$$

As a result:

$$k_2 \geq \eta + D \tag{3.24}$$

where η is a positive number, so if we choose k_2 as above, the system will be stable. Taking condition $S = 0$, the surface solution can be calculated as:

$$e_i(t) = e_i(0)\exp(-\lambda t). \tag{3.25}$$

Remark 1: The error trajectories of the attitude and position states approach the sliding surface in finite time and the tracking errors remains zero afterwards.

Remark 2: In equation (3.16) and (3.18), signum function, sgn

$$sgn(s) = \begin{cases} 1 & s > 0 \\ 0 & s = 0 \\ -1 & s < 0 \end{cases} \tag{3.26}$$

In practice, switching control law needs high frequency to switch across the surface which caused oscillates within neighborhood of the switching surface and it is called chattering. To prevent this phenomenon, various methods are used, such as using the *sat* function instead of *sgn*. This topic will be discussed at the end of this section.

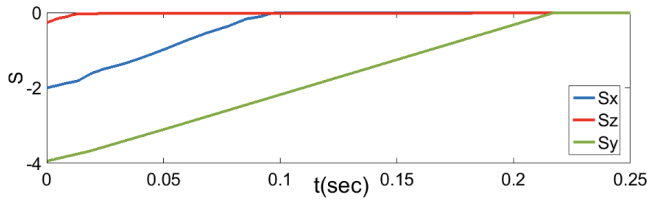

Figure 2: The sliding surface of the quadrotor position using first-order SMC

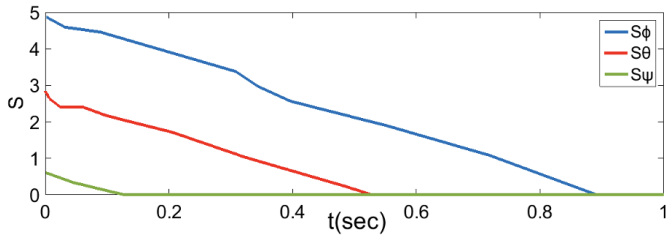

Figure 3: The sliding surface of the quadrotor attitude using first-order SMC

According to the equations mentioned in the previous section, the control inputs are obtained as follows:

$$U_1 = \left(-\frac{(I_{yy} - I_{zz})}{l}\dot{\theta}\dot{\psi} + \frac{J_{TP}}{l}\dot{\theta}\Omega + \frac{I_{xx}}{l}\ddot{\varphi}_d - \lambda_\varphi \frac{I_{xx}}{l}\dot{\tilde{\varphi}}\right) + \left(-k_\varphi \frac{I_{xx}}{l} sign\left(S_\varphi\right)\right) \tag{3.27}$$

$$U_2 = \left(-\frac{(I_{zz} - I_{xx})}{l}\dot{\varphi}\dot{\psi} - \frac{J_{TP}}{l}\dot{\varphi}\Omega + \frac{I_{yy}}{l}\ddot{\theta}_d - \lambda_\theta \frac{I_{yy}}{l}\dot{\tilde{\theta}}\right) + \left(-k_\theta \frac{I_{yy}}{l} sign\left(S_\theta\right)\right) \tag{3.28}$$

$$U_3 = \left(-\left(I_{xx} - I_{yy}\right)\dot{\varphi}\dot{\theta} + I_{zz}\ddot{\psi}_d - \lambda_\psi I_{zz}\lambda\dot{\tilde{\psi}}\right) + \left(-k_\psi I_{zz} sign\left(S_\psi\right)\right) \tag{3.29}$$

$$U_x = \left(\frac{m}{U_1}\right)\left(\ddot{x}_d - \lambda_x\dot{\tilde{x}}\right) + \left(-k_x s\left(\frac{m}{U_1}\right) sign\left(S_x\right)\right) \tag{3.30}$$

$$U_y = \left(\frac{m}{U_1}\right)\left(\ddot{y}_d - \lambda_y\dot{\tilde{y}}\right) + \left(-k_y\left(\frac{m}{U_1}\right) sign\left(S_y\right)\right) \tag{3.31}$$

$$U_z = \frac{m}{(\cos\theta\cos\varphi)}\left(g + \ddot{z}_d - \lambda_z\dot{\tilde{z}}\right) + \left(-k_z\frac{m}{(\cos\theta\cos\varphi)} sign\left(S_z\right)\right) \tag{3.32}$$

In the above control inputs, the first terms are as an equivalent part and the second one as a reaching part. The Control parameters are given in Table 2. These parameters are obtained based on trial and error.

Table 2: The Control parameters in the first-order SMC

Value	parameter	Value	parameter
3.4	k_φ	0.9	k_x
0.9	k_θ	2.2	k_y
0.98	k_ψ	1.5	k_z

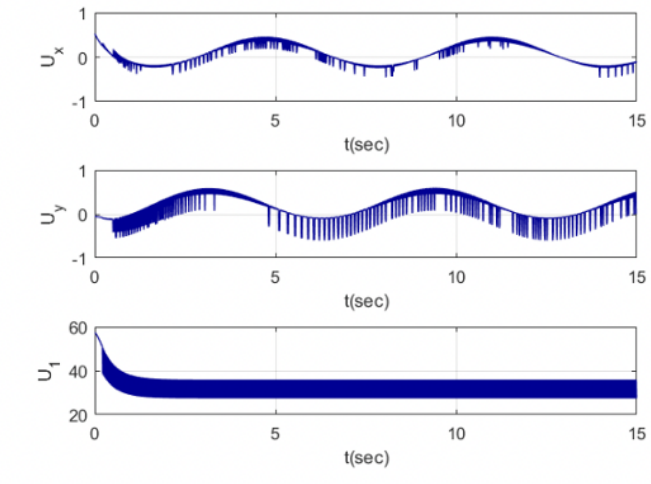

Figure 4: Quadrotor control commands using the first-order sliding mode control method

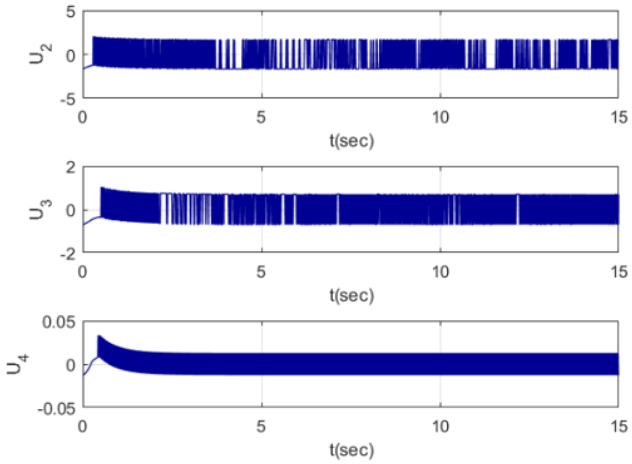

Figure 5: Quadrotor control commands using the first-order sliding mode control method

In this simulation, the control signals $-10 \leq u_x, u_y, u_2, u_3, u_4 \leq 10$ and $0 \leq u_1 \leq 50$ are considered. As it is clear from Figures 4 and 5, the simulation results indicate the chattering phenomenon in the control signal designed in the first-order sliding mode method as a result of the presence of the sign function, because this function in the control command forces the operator to switch momentarily. Since the implementation of the controller-sliding mode is not ideal, and the operators are not able to switch momentarily and do so with a delay, and also the value of the sliding variable, which is the weighted sum of the error, is not known with infinite accuracy, the chattering phenomenon occurs. In general, chattering is very undesirable because it has disadvantages such as high control activity, stimulation of unmodeled high-frequency dynamics, reduction of controller accuracy, increase in heat losses in electrical circuits, and increase in wear and tear in mechanical parts and actuators. These disadvantages reduce the efficiency of the system and may lead to instability. Some approaches to prevent chattering create a boundary layer in the vicinity of the discontinuity surface. A simple solution is to use a saturation function with a high gain (pseudo-sliding). In this paper, the following function is used.

$$\delta\nu(s.\delta) = \begin{cases} \operatorname{sgn}(s) & \text{if } |s| > \delta \\ \left(\frac{\delta}{|s|}\right)^{(q-1)} \operatorname{sgn}(s) & 0 < |s| < \delta \\ 0 & s = 0 \end{cases} \tag{3.33}$$

In the above equations, the tanh function can be used to obtain a close approximation to the sign function:

$$(s.\delta) = \tanh\left(\frac{s}{\delta}\right). \tag{3.34}$$

So that $\delta < 1$ is a small positive number which is defined as the pole of the curve. The results of the simulation are shown in Figures 6 and 7, which show that the chattering in the control commands has been removed and the tracking of the desired path has been done smoothly and without oscillation in the control commands.

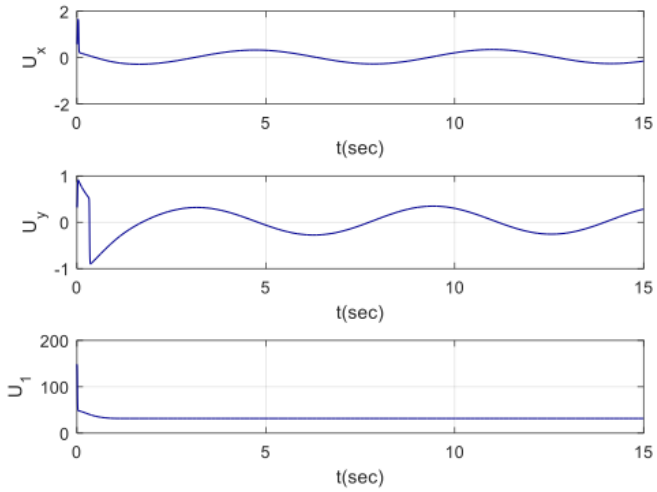

Figure 6: Quadrotor control commands with boundary layer

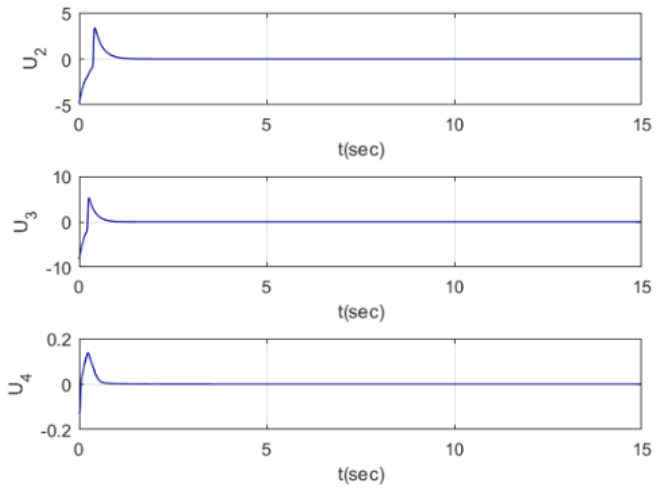

Figure 7: Quadrotor control commands with boundary layer

Table 3: Sensitivity analysis k_ϕ

k_ϕ	k_θ	k_ψ	k_x	k_y	k_z	e_ϕ
3.4	0.9	0.98	0.9	2.2	0.15	0.01
5.1	0.9	0.98	0.9	2.2	0.15	0.021
6.8	0.9	0.98	0.9	2.2	0.15	0.03
8.5	0.9	0.98	0.9	2.2	0.15	0.042

The convergence of the sliding surface of the followers to zero is clear in Figures 2 and 3. Figures 4 and 5 show the quadrotor control commands using the first-order sliding mode controller, where the chattering phenomenon is

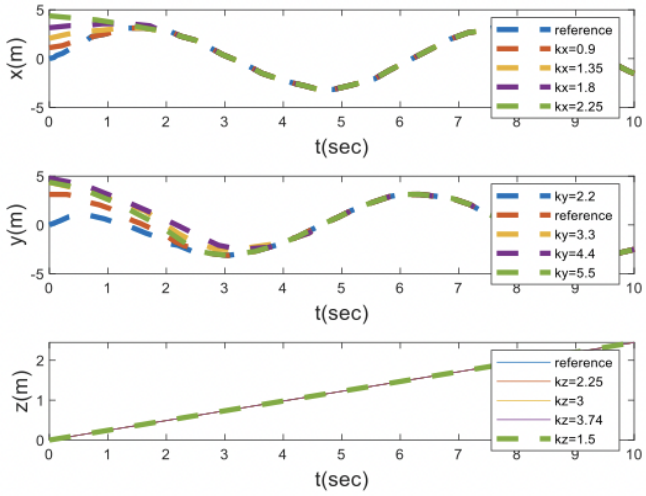

Figure 8: The position of the quadrotor using first-order SMC

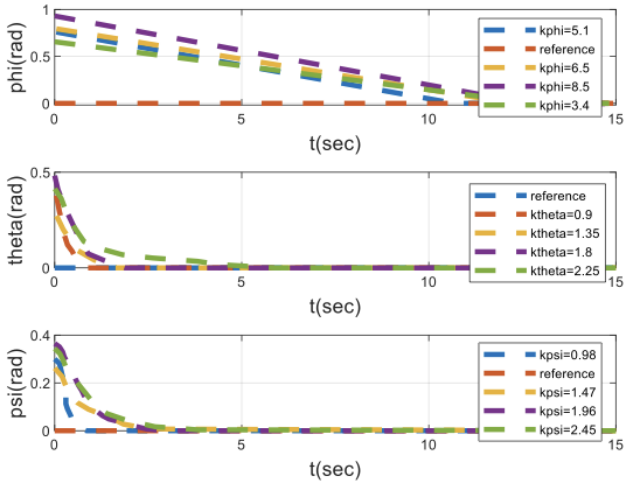

Figure 9: The attitude of the sliding surface of the quadrotor using first-order SMC

Table 4: Sensitivity analysis k_θ

k_ϕ	k_θ	k_ψ	k_x	k_y	k_z	e_θ
3.4	0.9	0.98	0.9	2.2	0.15	0.015
3.4	1.35	0.98	0.9	2.2	0.15	0.018
3.4	1.8	0.98	0.9	2.2	0.15	0.023
3.4	2.25	0.98	0.9	2.2	0.15	0.04

observed in the results. The results of the simulation to remove the chattering using the boundary layer in Figures 6 and 7 show the success of the applied method, and the tracking of the desired path is done smoothly and without fluctuations in the control commands, and the control commands are well converged in the desired time. Figures 8 and 9 represent the position and attitude of the quadrotor using first-order sliding mode controllers with a layer boundary, respectively. In these figures, the output for parameters $(k_\phi, k_\theta, k_\psi, k_x, k_y, k_z)$ with 1.5, 2, and 2.5 times the values presented in Table 2 are also shown. This sensitivity analysis for the control parameters shown in Tables 3-8 shows that the tracking error increased from 0.015 to 0.04 with the increase of the control parameters. Figure 10 also shows the prosperous tracking performance of the controller in three dimensions. In these figures, the effects of disturbances and the success of the controller in removing these disturbances are visible. The proposed controller has the following

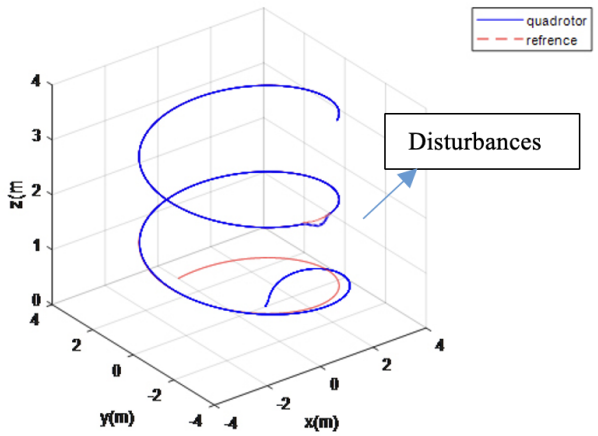

Figure 10: Three-dimensional diagram of quadrotor tracking using first-order SMC

merits: 1) convergence of the tracking error to zero, 2) stability of the closed-loop system. The chattering phenomenon is the main drawback of the method.

4 Terminal SMC

The emphasis of the terminal SMC is on reducing the convergence time sliding surface to zero. For this purpose, the sliding surface is considered as follows [3]:

$$S = x_1 + \lambda x_2^{\frac{\alpha}{\beta}} \tag{4.1}$$

where $\frac{1}{2} < \frac{\alpha}{\beta} < 1$, α and β are constant and positive numbers. For system (3.1) with the equation (3.32), if the control is designed as:

$$u = -b^{-1}(x)\left(f(x) + \lambda\frac{\beta}{\alpha}x_2^{2-\frac{\alpha}{\beta}} + \eta\text{sgn}(s)\right) \tag{4.2}$$

where $\eta > 0$, then the manifold (4.1) will be reached in finite time. Furthermore, the states x_1 and x_2 will converge to zero in finite time.

Proof. For the equation (4.1) , its derivative along the system dynamics (3.1) is:

$$\begin{aligned}\dot{s} &= \dot{x}_1 + \lambda\frac{\alpha}{\beta}x_2^{\frac{\alpha}{\beta}-1}\dot{x}_2 = x_2 + \lambda\frac{\alpha}{\beta}x_2^{\frac{\alpha}{\beta}-1}\left(f(x) + g(x) + b(x)u\right)\\ &= \lambda\frac{\alpha}{\beta}x_2^{\frac{\alpha}{\beta}-1}\left(g(x) - \eta\text{sgn}(s)\right)\end{aligned}$$

$$s\dot{s} = \lambda\frac{\alpha}{\beta}x_2^{\frac{\alpha}{\beta}-1}\left(g(x)s - \eta\text{sgn}(s)s\right) \leq -\lambda\frac{\alpha}{\beta}x_2^{\frac{\alpha}{\beta}-1}\eta|s|$$

where $1 < \frac{\alpha}{\beta} < 2$, there is $x_2^{\frac{\alpha}{\beta}-1} > 0$ for $x_2 \neq 0$. Let $\xi(x_2) = \lambda\frac{\alpha}{\beta}x_2^{\frac{\alpha}{\beta}-1}\eta$. Then:

$$s\dot{s} \leq -\xi(x_2)|s| \text{ for } x_2 \neq 0 \tag{4.3}$$

$$\xi(x_2) > 0. \tag{4.4}$$

Therefore, for the $x_2 > 0$, the condition for Lyapunov stability is satisfied. Substituting equation (3.17) into system (2.6) gives the result:

$$\dot{x}_2 = -\frac{1}{\lambda}\frac{\beta}{\alpha}x_2^{2-\frac{\alpha}{\beta}} + g(x) - \eta\text{sgn}(s). \tag{4.5}$$

For $x_2 = 0$,

$$\dot{x}_2 = -\frac{1}{\lambda}\frac{\beta}{\alpha}x_2^{2-\frac{\alpha}{\beta}} + g(x) - \eta\text{sgn}(s). \tag{4.6}$$

For $s > 0$, $\dot{x}_2 \leq \eta$ and for $s < 0$, $\dot{x}_2 \geq \eta$, showing that $x_2 = 0$ is not an attractor and there exists a vicinity of $x_2 = 0$ such that for a small $\varepsilon > 0$ such that $|x_2| < \varepsilon$, there are $\dot{x}_2 \leq -\eta$ for $s > 0$ and $\dot{x}_2 \geq \eta$ for $s < 0$. The crossing of the trajectory from the boundary of the vicinity $x_2 = \varepsilon$ to $x_2 = -\varepsilon$ for $s > 0$, and from $x_2 = -\varepsilon$ to $x_2 = \varepsilon$ for $s < 0$ occurs in finite time. For other regions where $|x_2| > \varepsilon$, it can be concluded from (3.1) that the switching line $s = 0$ can be reached in the finite time since we have $\dot{x}_2 \leq -\eta$ for $s > 0$ and $\dot{x}_2 \geq \eta$ for $s < 0$. Therefore, it is concluded that the sliding mode $s = 0$ can be reached from anywhere in finite time. Therefore, the NTSM manifold (4.1) can be reached in a finite time. The states in the sliding mode will reach zero in finite time. This completes the proof. □
The reach time is obtained by setting the sliding surface equal to zero and deriving from it:

$$t_s = \frac{-x_i^{(1-\frac{\beta}{\alpha})}(t_r)}{\lambda_i^{\frac{q}{p}}(1-\frac{\alpha}{\beta})}, \tag{4.7}$$

where t_r is the time that s reaches zero. Table 9 shows the values t_s.

Table 5: Reaching time

$t_s(x)$	$t_s(y)$	$t_s(z)$	$t_s(\varphi)$	$t_s(\theta)$	$t_s(\psi)$
0.5(s)	2(s)	0(s)	4.1(s)	2(s)	1(s)

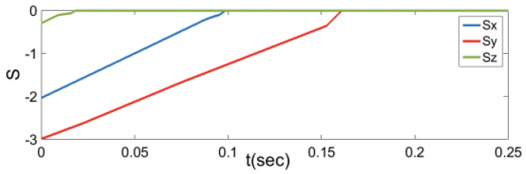

Figure 11: Sliding surface of quadrotor position using terminal SMC

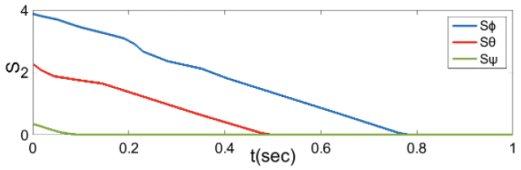

Figure 12: The sliding surface of quadrotor attitude using terminal SMC

u_{eq} is as equivalent term, and u_r as reaching one.

$$u_r = k\text{sign}(S). \tag{4.8}$$

As a result, using the terminal SMC, the control commands for the mentioned quadrotor are as follow:

$$U_1 = \frac{m}{(\cos\theta\cos\varphi - g)} \frac{\left[-\dddot{\tilde{z}} + \dddot{z}_d \lambda_z \frac{\alpha}{\beta} \dot{\tilde{z}}^{(\frac{\alpha}{\beta}-1)}\right]}{\left[\lambda_z \frac{\alpha}{\beta} \dot{\tilde{z}}^{(\frac{\alpha}{\beta}-1)}\right]} + k_z \text{sign}(S_z)$$

$$U_2 = \frac{-\frac{I_x}{L}\left[\dddot{\tilde{\varphi}} + \lambda_\varphi \frac{\alpha}{\beta} \dot{\tilde{\varphi}}^{(\frac{\alpha}{\beta}-1)} \left(\frac{(I_y - I_z)}{I_x}\dot{\theta}\dot{\psi} - \frac{J_{TP}}{I_x}\dot{\theta}\Omega - \ddot{\varphi}_d\right)\right]}{\left[\lambda_\varphi \frac{\alpha}{\beta} \dot{\tilde{\varphi}}^{(\frac{\alpha}{\beta}-1)}\right]} + k_\varphi \text{sign}(S_\varphi)$$

$$U_3 = -\left(\frac{I_y}{L}\right) \frac{\left[\dddot{\tilde{\theta}} + \lambda_\theta \frac{\alpha}{\beta} \dot{\tilde{\theta}}^{(\frac{\alpha}{\beta}-1)} \left(\frac{(I_z - I_x)}{I_y}\dot{\varphi}\dot{\psi} + \frac{J_{TP}}{I_y}\dot{\varphi}\Omega - \ddot{\theta}_d\right)\right]}{\left[\lambda_\theta \frac{\alpha}{\beta} \dot{\tilde{\theta}}^{(\frac{\alpha}{\beta}-1)}\right]} + k_\theta \text{sign}(S_\theta)$$

$$U_4 = -I_z \frac{\left[\dot{\tilde{\psi}} + \lambda_\psi \frac{\alpha}{\beta} \dot{\tilde{\psi}}^{(\frac{\alpha}{\beta}-1)} \left(\frac{(I_x - I_y)}{I_z}\dot{\varphi}\dot{\theta} - \ddot{\psi}_d\right)\right]}{\left[\lambda_\psi \frac{\alpha}{\beta} \dot{\tilde{\psi}}^{(\frac{\alpha}{\beta}-1)}\right]} + k_\psi \text{sign}(S_\psi)$$

$$U_x = -\left(\frac{m}{U_1}\right) \frac{\left[\lambda_x \frac{\alpha}{\beta} \dot{\tilde{x}}^{(\frac{\alpha}{\beta}-1)}(-\ddot{x}_d) + \dot{\tilde{x}}\right]}{\left[\lambda_x \frac{\alpha}{\beta} \dot{\tilde{x}}^{(\frac{\alpha}{\beta}-1)}\right]} + k_x \text{sign}(S_x)$$

$$U_y = -\left(\frac{m}{U_1}\right) \frac{\left[\dot{\tilde{y}} + \lambda_y \frac{\alpha}{\beta} \dot{\tilde{y}}^{(\frac{\alpha}{\beta}-1)}(-\ddot{y}_d)\right]}{\left[\lambda_y \frac{\alpha}{\beta} \dot{\tilde{y}}^{(\frac{\alpha}{\beta}-1)}\right]} + k_y \text{sign}(S_y)$$

Table 6: Fixed parameter values in the design of terminal SMC

Value	parameter	Value	parameter
11	k_φ	21	k_x
11	k_θ	17	k_y
11	k_ψ	21	k_z
0.75	$\frac{\alpha}{\beta}$	0.1	δ

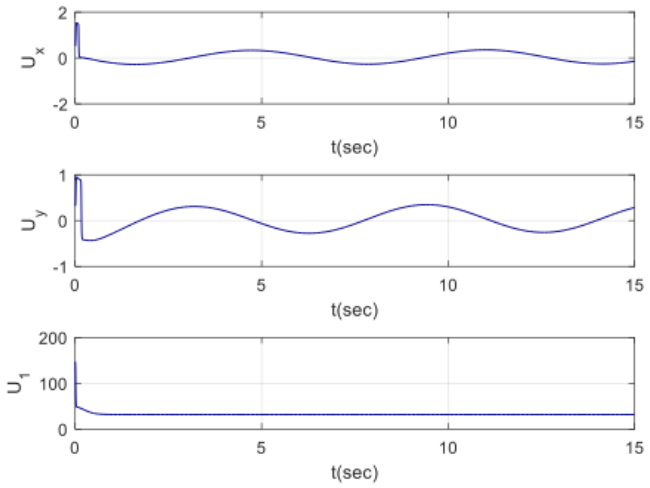

Figure 13: Quadrotor control commands using the terminal sliding mode

According to Figures 11 and 12, the sliding surfaces reach zero in finite time. Figures 13 and 14 show the quadrotor control commands. Figures 15 and 16 represent the position and attitude of the quadrotor using nonsingular terminal sliding mode controllers, respectively. In these figures, the outputs for k 1.5, 2, and 2.5 times the control parameters presented in Table 10 are also shown. The results of the sensitivity analysis of the control parameters are shown in Tables 11-16, which show that the simulation error and the value of t_r increase with the increase of the control parameters. Figure 17 also shows the effective 3-D tracking of the plant. The simulation results and the calculation of the reaching time of the states showed that the reaching time in the terminal controller is less than the first-order one.

5 Super Twisting SMC

ST-SMC is designated to decrease the chattering phenomena for a quadrotor with a relative degree of one. The variable dynamics of the sliding surface can be written as follows:

$$\dot{s} = \Phi(t, x) + \Upsilon(t, x)u \tag{5.1}$$

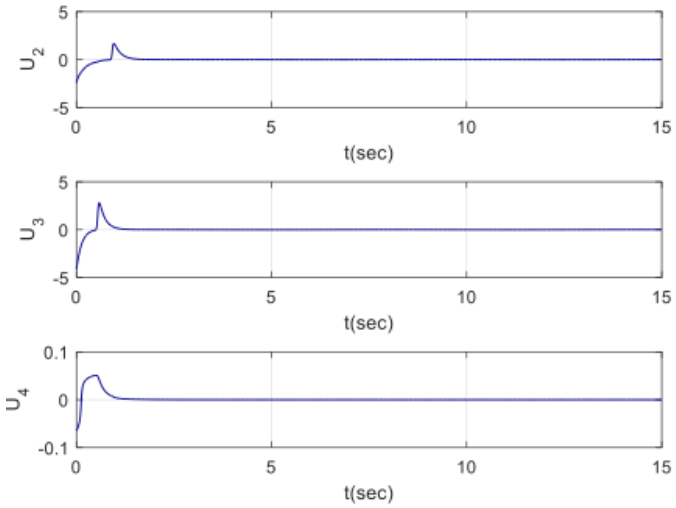

Figure 14: Quadrotor control commands using the terminal sliding mode

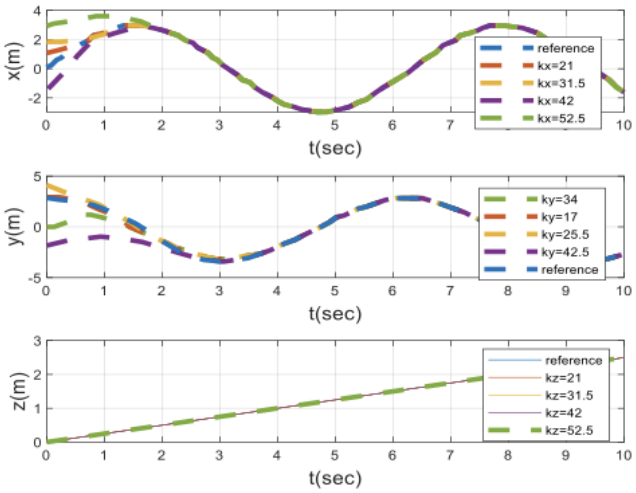

Figure 15: The position of the quadrotor using the terminal SMC

with limited conditions $|\Phi(t,x)| \leq \Phi$, $0 < \Gamma_m \leq \Upsilon(t,x) \leq \Gamma_M$ and $|S| \leq S_0$. So Γ_m, Γ_M, and Φ are positive constant values. Control inputs in ST-SMC are designed as follows:

$$u = u_1 + u_2 \tag{5.2}$$

where:

$$\dot{u}_1 = \begin{cases} -u & |u| > 1 \\ -W\text{sign}(s) & |u| \leq 1 \end{cases} \tag{5.3}$$

$$u_2 = \begin{cases} -\lambda |s_0|^{\rho} \text{sign}(s) & |s| > s_0 \\ -\lambda |s|^{\rho} \text{sign}(s) & |s| \leq s_0 \end{cases} \tag{5.4}$$

Sufficient and appropriate conditions for finite time convergence are as follows:

$$W > \frac{\Phi}{\Gamma_m} > 0 \tag{5.5}$$

$$\lambda^2 \geq \frac{4\phi\Gamma_M(W+\Phi)}{\Gamma_m^3(W-\Phi)}. \tag{5.6}$$

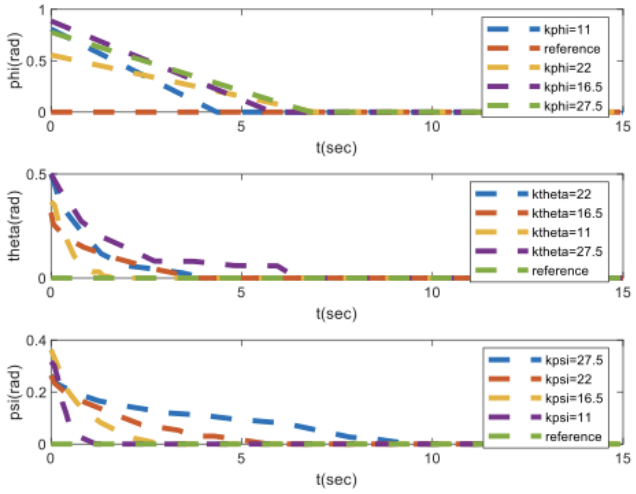

Figure 16: The attitude of the quadrotor using the terminal SMC

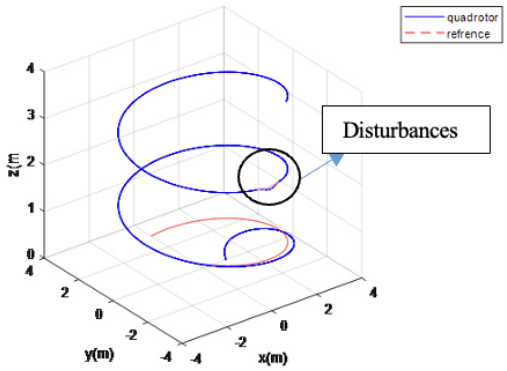

Figure 17: Three-dimensional diagram of quadrotor tracking using terminal SMC

This algorithm does not need the sign of the time derivative of the sliding surface to create a smooth control. For $\rho = 1$, the algorithm converges exponentially to the origin. For the systems where $s_0 = \infty$ and there is no limitation in the control, the algorithm can be simplified as follows [8, 13, 17]:

$$u(t) = -\lambda |s|^{\rho} \text{sign}(s) + u_1 \tag{5.7}$$

$$u = -\lambda |s|^{\rho} \text{sign}(s) + k \int \text{sign}(S). \tag{5.8}$$

To design the ST-SMC, the slide surface is considered for each of the control inputs as the first-order SMC. Thus u_{eq} is attained for each of the control commands like U_{eq} in the first-order SMC. However, U_r is assumed according

to Equation (2.15).

$$
\begin{aligned}
U_1 &= \frac{m}{(\cos\theta\cos\varphi)}\left(g+\ddot{z}_d-\lambda_z\dot{\tilde{z}}-k_{z1}|S_z|^{\rho}\text{sign}(S_z)-k_{z2}\int\text{sign}(S_z)\right)\\
U_2 &= \frac{I_x}{L}\left(-\frac{(I_y-I_z)}{I_x}\dot{\theta}\dot{\psi}+\frac{J_{TP}}{I_x}\dot{\theta}\Omega+\ddot{\varphi}_d-\lambda_\varphi\dot{\tilde{\varphi}}-k_{\varphi1}|S_\varphi|^{\rho}\text{sign}(S_\varphi)-k_{\varphi2}\int\text{sign}(S_\varphi)\right)\\
U_3 &= \left(\frac{I_y}{L}\right)\left(-\frac{(I_z-I_x)}{I_y}\dot{\varphi}\dot{\psi}-\frac{J_{TP}}{I_y}\dot{\varphi}\Omega+\ddot{\theta}_d-\lambda_\theta\dot{\tilde{\theta}}-k_{\theta1}|S_\theta|^{\rho}\text{sign}(S_\theta)-k_{\theta2}\int\text{sign}(S_\theta)\right)\\
U_4 &= I_z\left(-\frac{(I_x-I_y)}{I_z}\dot{\varphi}\dot{\theta}+\ddot{\psi}_d-\lambda_\psi\dot{\tilde{\psi}}-k_{\psi1}|S_\psi|^{\rho}\text{sign}(S_\psi)-k_{\psi2}\int\text{sign}(S_\psi)\right)\\
U_x &= \left(\frac{m}{U_1}\right)\left(\ddot{x}_d-\lambda_x\dot{\tilde{x}}-k_{x1}|S_x|^{\rho}\text{sign}(S_x)-k_{x2}\int\text{sign}(S_x)\right)\\
U_y &= \left(\frac{m}{U_1}\right)\left(\ddot{y}_d-\lambda_y\dot{\tilde{y}}-k_{y1}|S_y|^{\rho}\text{sign}(S_y)-k_{y2}\int\text{sign}(S_y)\right)
\end{aligned}
\tag{5.9}
$$

Table 7: Parameter values in the design of ST-SMC

Value	parameter	Value	parameter
0.9	k_φ	22	k_x
1.1	k_θ	16.02	k_y
1.52	k_ψ	21	k_z
		0.1	δ

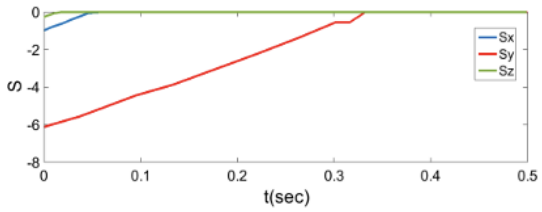

Figure 18: The sliding surface of the quadrotor position using ST-SMC

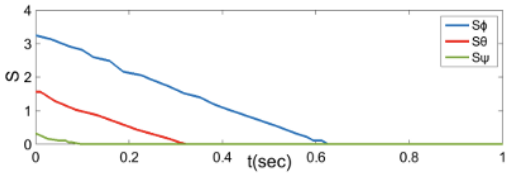

Figure 19: The sliding surface of the quadrotor attitude using ST-SMC

According to Figures 18 and 19, the sliding surfaces reach zero in finite time. Figures 20 and 21 represent quadrotor control commands as depicted in equation (5.9), and Figures 22 and 23 represent the position and attitude of the quadrotor using ST-SMC, respectively. Also, in these figures, the outputs are plotted for 1.5, 2, and 2.5 times the values presented in Table 17. The sensitivity analysis of the control parameters is shown in Tables 18-23, which shows that the simulation error increases with the increase in the values of the control parameters. Figure 24 also shows the productive 3-D presentation of the planned methodology. This approach decreases chattering phenomena and increases by about 5% of overshoot.

6 Nonsingular Terminal Super Twisting SMC

In this controller, the slide surface is considered to be the same as the slide surface of the nonsingular terminal SMC [8]. As a result, u_{eq} is equal to one obtained in the terminal SMC. u_{dis} is also the same as the one stated in the

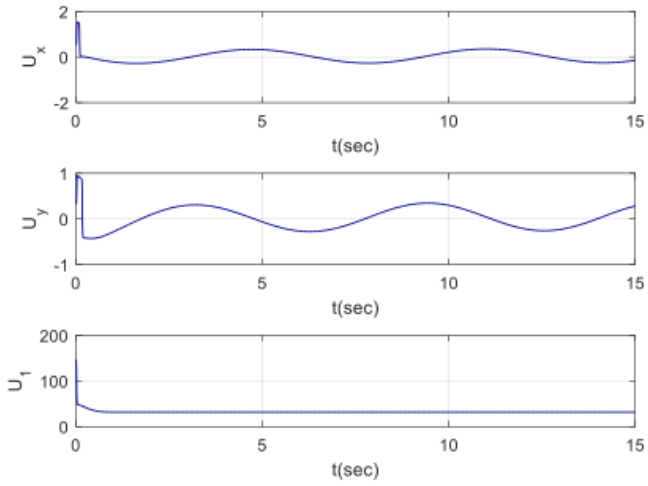

Figure 20: Quadrotor control commands using the ST-SMC

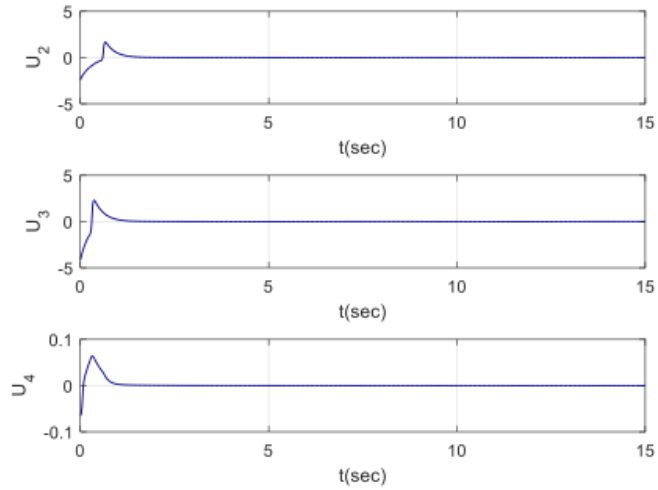

Figure 21: Quadrotor control commands using the ST-SMC

ST-SMC. Therefore, using the nonsingular terminal super twisting sliding mode controller, the control inputs for the plant were achieved as follows:

$$U_1 = \frac{m}{(\cos\theta\cos\varphi - g)} \frac{\left[-\dot{\tilde{z}} + \ddot{z}_d \lambda_z \frac{\alpha}{\beta} \dot{\tilde{z}}^{(\frac{\alpha}{\beta}-1)}\right]}{\left[\lambda_z \frac{\alpha}{\beta} \dot{\tilde{z}}^{(\frac{\alpha}{\beta}-1)}\right]} + k_{z1}|S_z|^{\rho}\text{sign}(S_z) + k_{z2}\int \text{sign}(S_z)$$

$$U_2 = \frac{-\frac{I_x}{L}\left[\dot{\tilde{\varphi}} + \lambda_\varphi \frac{\alpha}{\beta} \dot{\tilde{\varphi}}^{(\frac{\alpha}{\beta}-1)} \left(\frac{(I_y - I_z)}{I_x}\dot{\theta}\dot{\psi} - \frac{J_{TP}}{I_x}\dot{\theta}\Omega - \ddot{\varphi}_d\right)\right]}{\left[\lambda_\varphi \frac{\alpha}{\beta} \dot{\tilde{\varphi}}^{(\frac{\alpha}{\beta}-1)}\right]} + k_\varphi|S_\varphi|^{\rho}\text{sign}(S_\varphi) - k_\varphi\int \text{sign}(S_\varphi)$$

$$U_3 = -\left(\frac{I_y}{L}\right) \frac{\left[\dot{\tilde{\theta}} + \lambda_\theta \frac{\alpha}{\beta} \dot{\tilde{\theta}}^{(\frac{\alpha}{\beta}-1)} \left(\frac{(I_z - I_x)}{I_y}\dot{\varphi}\dot{\psi} + \frac{J_{TP}}{I_y}\dot{\varphi}\Omega - \ddot{\theta}_d\right)\right]}{\left[\lambda_\theta \frac{\alpha}{\beta} \dot{\tilde{\theta}}^{(\frac{\alpha}{\beta}-1)}\right]} + k_\theta|S_\theta|^{\rho}\text{sign}(S_\theta) - k_\theta\int \text{sign}(S_\theta)$$

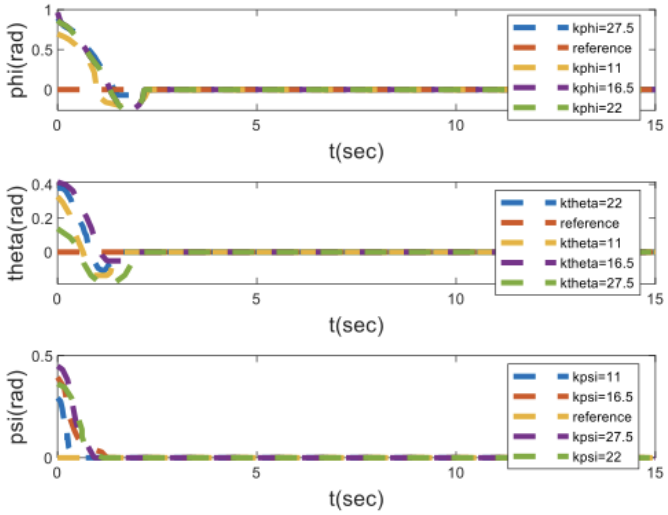

Figure 22: The attitude of the quadrotor using the ST-SMC

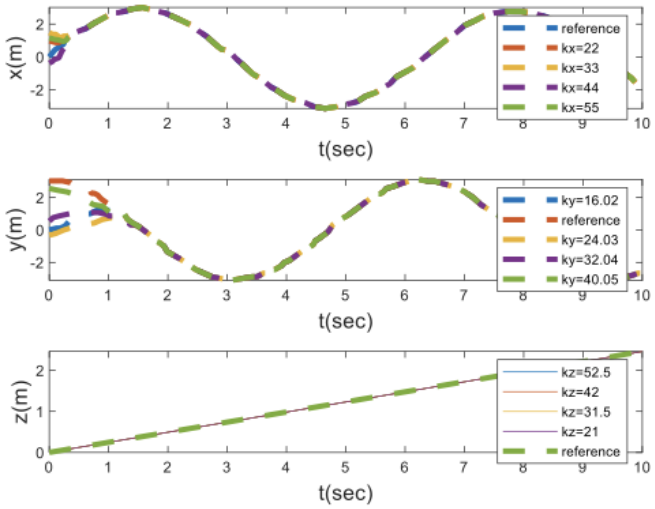

Figure 23: The position of the sliding surface of the quadrotor using the ST-SMC

$$U_4 = -I_z \frac{\left[\dddot{\tilde{\psi}} + \lambda_\psi \frac{\alpha}{\beta} \ddot{\tilde{\psi}}^{(\frac{\alpha}{\beta}-1)} \left(\frac{(I_x - I_y)}{I_z} \dot{\varphi}\dot{\theta} - \ddot{\psi}_d\right)\right]}{\left[\lambda_\psi \frac{\alpha}{\beta} \dot{\tilde{\psi}}^{(\frac{\alpha}{\beta}-1)}\right]} + k_\psi |S_\psi|^\rho \text{sign}(S_\psi) - k_\psi \int \text{sign}(S_\psi)$$

$$U_x = -\left(\frac{m}{U_1}\right) \frac{\left[\lambda_x \frac{\alpha}{\beta} \dot{\tilde{x}}^{(\frac{\alpha}{\beta}-1)} (-\ddot{x}_d) + \dddot{\tilde{x}}\right]}{\left[\lambda_x \frac{\alpha}{\beta} \ddot{\tilde{x}}^{(\frac{\alpha}{\beta}-1)}\right]} + k_x |S_x|^\rho \text{sign}(S_x) - k_x \int \text{sign}(S_x)$$

$$U_y = -\left(\frac{m}{U_1}\right) \frac{\left[\dddot{\tilde{y}} + \lambda_y \frac{\alpha}{\beta} \ddot{\tilde{y}}^{(\frac{\alpha}{\beta}-1)} (-\ddot{y}_d)\right]}{\left[\lambda_y \frac{\alpha}{\beta} \ddot{\tilde{y}}^{(\frac{\alpha}{\beta}-1)}\right]} - k_y |S_y|^\rho \text{sign}(S_y) - k_y \int \text{sign}(S_y)$$

The results of the simulation of four controllers showed that the outputs converge to the desired value. The convergence time in the non-singular super-twisting terminal controller is less than in the other three methods. The

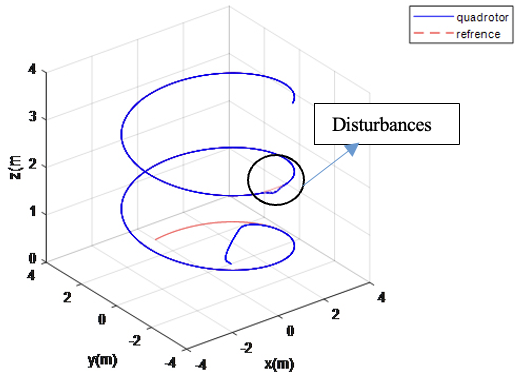

Figure 24: Three-dimensional diagram of quadrotor tracking ST-SMC

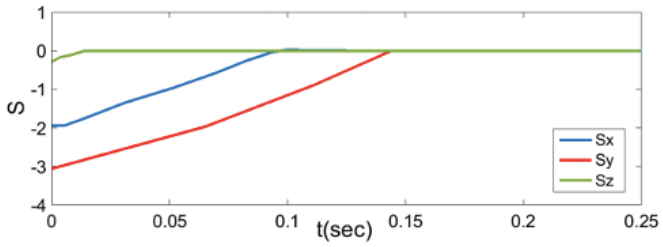

Figure 25: The sliding surface of the quadrotor position using nonsingular terminal super twisting sliding mode

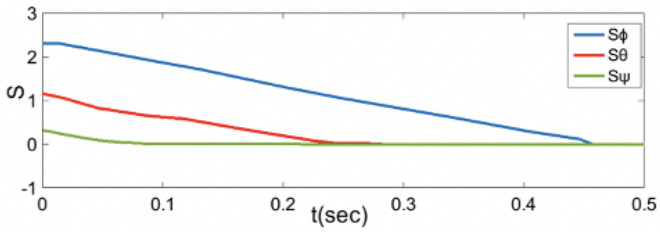

Figure 26: The sliding surface of the quadrotor attitude using nonsingular terminal super twisting sliding mode

sensitivity analysis also showed that by increasing the value of the control parameters, the simulation error and reaching time increase. These results showed that the super twisting terminal sliding mode controller is less sensitive to the change of control parameters than other controllers. Therefore, the quadrotor position and attitude controller were made using this control method.

7 Formation Control

In the leader-follower formation procedure, 1) the leader first follows a predetermined path; 2) the leader position is the input of the formation control for the following quadrotors [**?** **?**]. As shown in Figure 32, λ is the distance from the center of leader mass to the center of follower mass, and φ is the angle between the x-axis of the leader and λ line. Figure 33 also shows the block diagram of the quadrotor formation control.

$$\begin{cases} \lambda_x = -(x_L - x_F)\cos\psi_L - (y_L - y_F)\sin\psi_L \\ \lambda_y = -(x_L - x_F)\sin\psi_L - (y_L - y_F)\cos\psi_L \end{cases} \tag{7.1}$$

$$\begin{aligned} \lambda_x^d &= \lambda\cos\varphi \\ \lambda_y^d &= \lambda\sin\varphi \end{aligned} \tag{7.2}$$

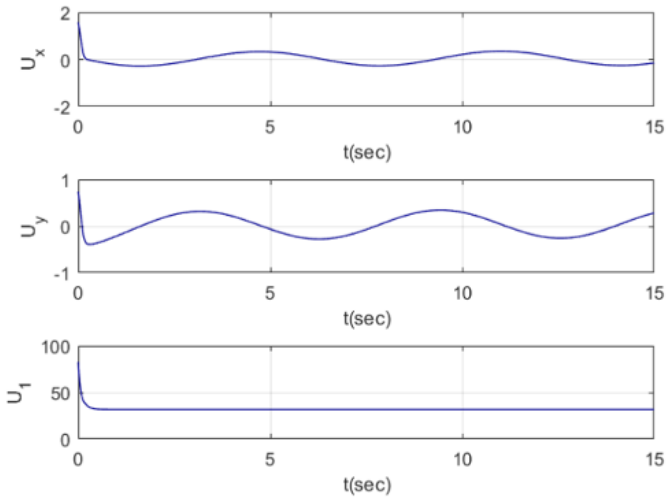

Figure 27: Quadrotor control commands using the terminal ST-SMC

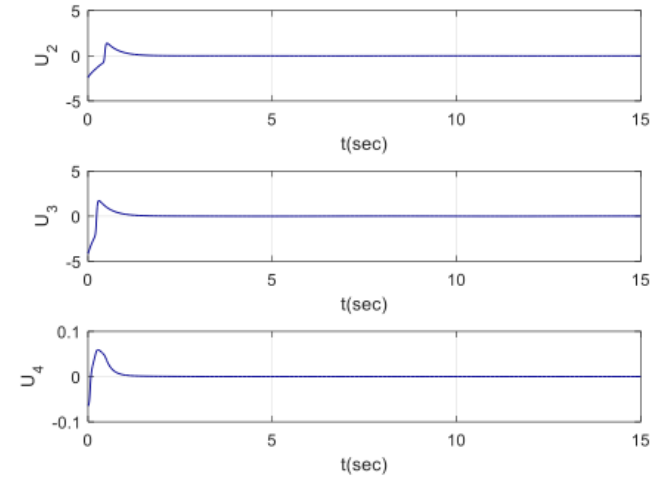

Figure 28: Quadrotor control commands using the terminal ST-SMC

Therefore, the formation error can be defined as follows:

$$\begin{cases} e_x = \lambda_x^d - \lambda_x \\ e_y = \lambda_y^d - \lambda_y \\ e_\psi = \psi_F - \psi_L \end{cases} \tag{7.3}$$

Considering that λ^d and ϕ^d have constant values, as a result, λ_x^d and λ_y^d have constant values and their derivatives $\dot{\lambda}_x^d$ and $\dot{\lambda}_y^d$ are zero. In the following, $\dot{\lambda}_x$ and $\dot{\lambda}_y$ are obtained by deriving relations and defining the translational dynamics in the x-y plane. The transition dynamics on the x-y plane are also defined as follows:

$$\begin{cases} \dot{x}_i = v_{ix}\cos\psi_i - v_{iy}\sin\psi_i \\ \dot{y}_i = v_{ix}\sin\psi_i + v_{iy}\cos\psi_i \\ \dot{\psi}_L = \omega_L \end{cases} \tag{7.4}$$

Subscript i represents leader ($i = L$) or follower ($i = F$). Where $\dot{x}_i$ and $\dot{y}_i$ are velocity in the ground coordinate system. ψ_i is the angle between the x-axis direction of the fuselage system and the ground coordinate system, and v_{ix}

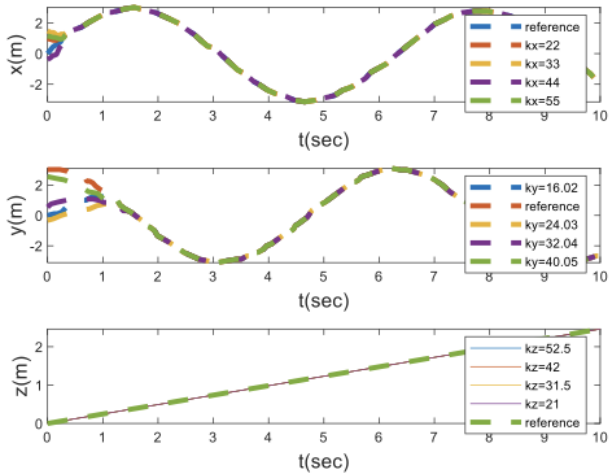

Figure 29: The position of the quadrotor using the terminal ST-SMC

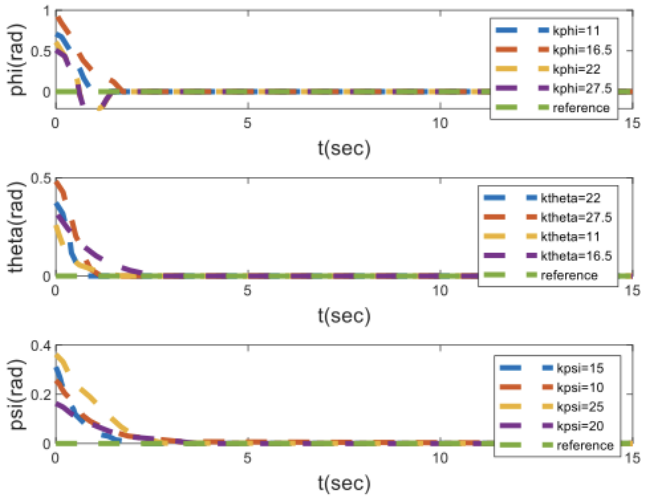

Figure 30: The attitude of the quadrotor using the terminal ST-SMC

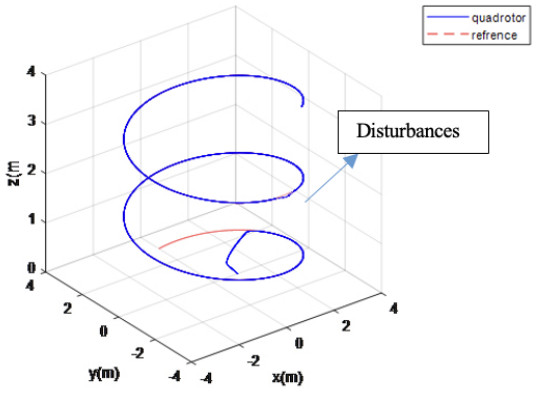

Figure 31: Three-dimensional diagram of quadrotor tracking using terminal ST-SMC

and v_{iy} are the velocity in the fuselage coordinate system which are gotten as:

$$\begin{cases} v_{ix} = \dot{x}_i \cos\psi_i + \dot{y}_i \sin\psi_i \\ v_{iy} = -\dot{x}_i \sin\psi_i + \dot{y}_i \cos\psi_i \end{cases} \tag{7.5}$$

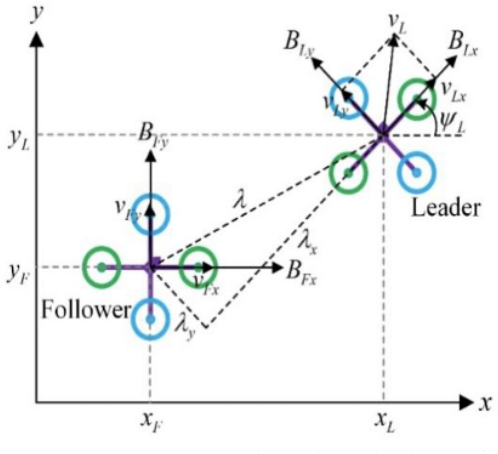

Figure 32: Quadrotor formation in x-y plane

By placing relations (7.1), (7.2), (7.4), and (7.5) in (7.3), the following relations are obtained:

$$\begin{cases} \dot{e}_x = -(\lambda_y^d - e_y)\omega_L - v_{Fx}\cos e_\psi + v_{Fy}\sin e_\psi + v_{Lx} \\ \dot{e}_y = (\lambda_x^d - e_x)\omega_L - v_{Fx}\sin e_\psi - v_{Fy}\cos e_\psi + v_{Ly} \\ \dot{e}_\psi = \omega_F - \omega_L \end{cases} \tag{7.6}$$

The State Space Representation can be depicted below:

$$\dot{x} = M(x) + N(x)v \tag{7.7}$$

where x is the state vector and v is the control input, and $M(x)$ and $N(x)$ are all expressed as below.

$$x = \begin{bmatrix} e_x & e_y & e_\psi \end{bmatrix}^T \tag{7.8}$$

$$v = \begin{bmatrix} v_{Fx} & v_{Fy} & \omega_F \end{bmatrix}^T \tag{7.9}$$

$$M(x) = \begin{bmatrix} e_y\omega_L + v_{Lx} - \omega_L\lambda_y^d \\ -e_x\omega_L + v_{Ly} + \omega_L\lambda_x^d \\ -\omega_L \end{bmatrix} \tag{7.10}$$

$$N(x) = \begin{bmatrix} -\cos e_\psi & \sin e_\psi & 0 \\ -\sin e_\psi & -\cos e_\psi & 0 \\ 0 & 0 & 1 \end{bmatrix} \tag{7.11}$$

To guarantee the convergence of the formation error to zero, an integral SMC is a candidate to reach the formation. The sliding surface is as:

$$S = k_f \int x\,dt + x \tag{7.12}$$

which k_f is a constant matrix that defines later. The SMC integral consists of two parts: equivalent term and reaching one as in equation (7.13).

$$v = v_{eq} + v_r. \tag{7.13}$$

The equivalent term is attained in equation (7.14).

$$v_{eq} = N^{-1}(x)(-M(x) - k_f x) \tag{7.14}$$

To ensure that the system is kept at the surface of $s = 0$ considering the perturbations, it can be deliberated as follows.

$$s = \dot{x} + k_f x = M(x) + N(x)v_{eq} + k_f x = -L\,\mathrm{sgn}(s) \tag{7.15}$$

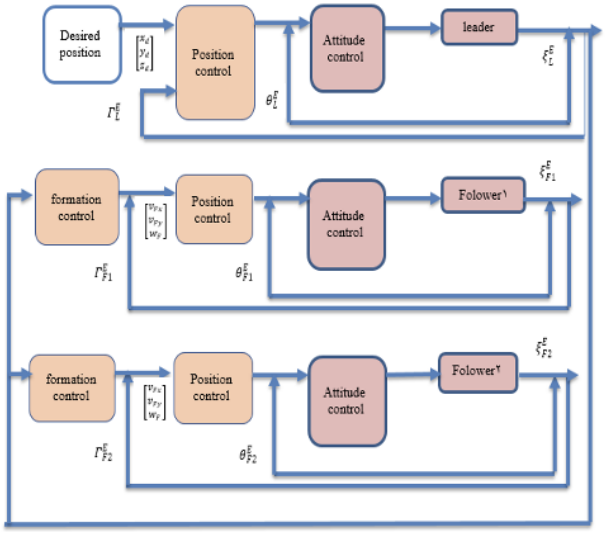

Figure 33: Quadrotor formation control block diagram

where L is a positive constant. Then the reaching term is achieved as follows:

$$v_r = -L\,\mathrm{sgn}(s) \tag{7.16}$$

According to the mentioned relations in (7.14), (7.15), and (7.16), the formation control command was gained as (7.17).

$$v = N^{-1}(x)(-M(x) - k_f x - L\,\mathrm{sgn}(s)). \tag{7.17}$$

To demonstrate the stability of the formation control, the succeeding Lyapunov function is a candidate: $V = \frac{1}{2}s^T s$. The time derivative of the above Lyapunov function holds below.

$$\dot{V} = s^T(M(x) + N(x)v + k_f x) = s^T(-L\,\mathrm{sgn}(s)) < -L|s| < 0. \tag{7.18}$$

Therefore, if $L > 0$, it is ensured that V is a definite negative and consequently, the states of the system will reach to the surface of $s = 0$ in a limited time and will remain on it. In the following, the results of simulation in three missions are specified and their specifications are settled in table 32. It is assumed that the wind as disturbances is considered as follows:

$$V_x = 0.5\sin(0.1t - \pi) \tag{7.19}$$

$$V_y = 0.5\sin(0.1t - \pi) \tag{7.20}$$

Table 8: Characteristics of the three missions

Characteristics of formation geometry	Desired position	Number of quadrotors
$\begin{cases}\lambda_1 = 2, \phi_1 = \pi/3\\ \lambda_2 = 2, \phi_2 = 2\pi/3\end{cases}$	$\begin{cases}x_d = 3\sin t\\ y_d = 3\cos t\\ z_d = \frac{1}{4}t\end{cases}$	3
$\begin{cases}\lambda_1 = 2, \phi_1 = \pi/3\\ \lambda_2 = 4, \phi_2 = \pi/3\end{cases}$	$\begin{cases}x_d = \frac{1}{4}t\\ y_d = 3\cos t\\ z_d = \frac{1}{4}t\end{cases}$	3
$\begin{cases}\lambda_1 = 2, \phi_1 = \pi/3\\ \lambda_2 = 4, \phi_2 = \pi/3\\ \lambda_3 = 6, \phi_3 = \pi/3\\ \lambda_4 = 8, \phi_4 = \pi/3\end{cases}$	$\begin{cases}x_d = \frac{1}{4}t\\ y_d = 3\cos t\\ z_d = \frac{1}{4}t\end{cases}$	5

In the first mission, three quadrotors in a triangular formation shape cross the spiral path. The simulation results for the first mission, are shown in Figures 34, 35, and 36. Figures 34 and 35 represent the position and attitude of

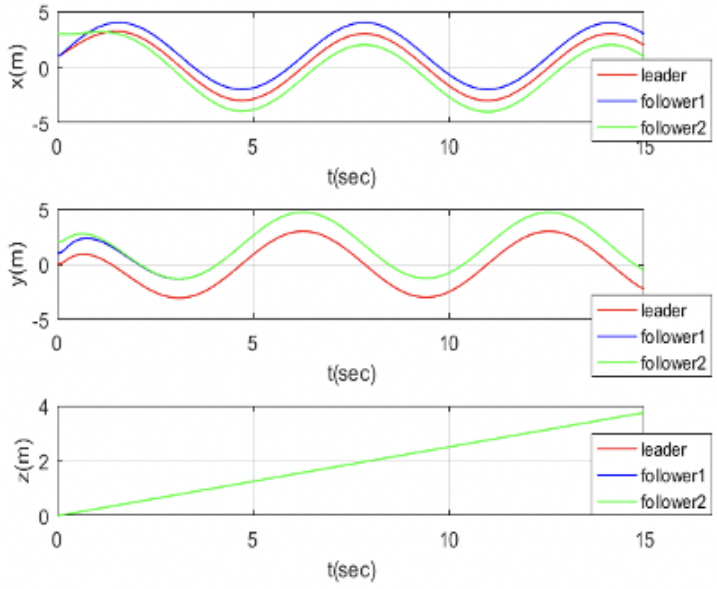

Figure 34: The position of the leader and the followers along the spiral path

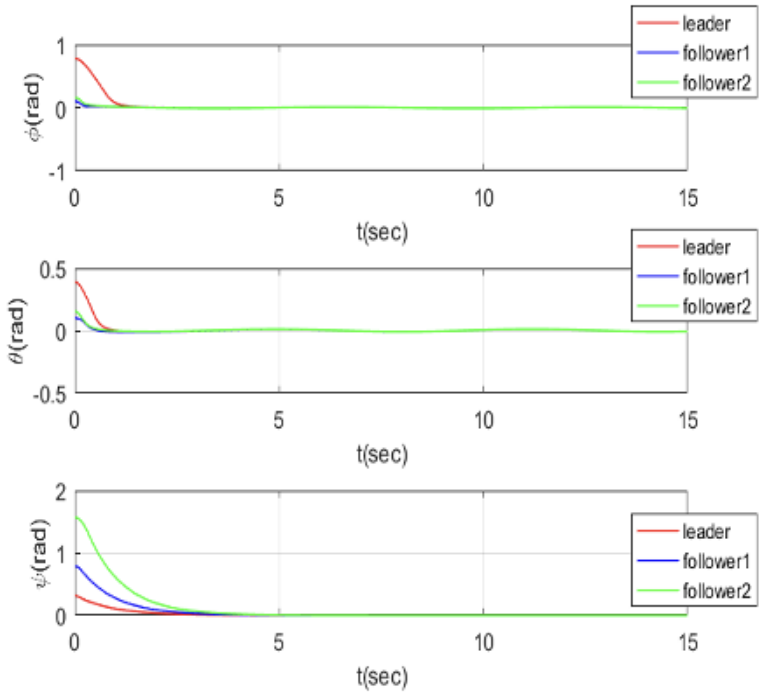

Figure 35: Response of attitude of three quadrotors along the spiral path

three quadrotors respectively. Figure 36 shows the three-dimensional diagram of three quadrotors. These figures show that the formation control of these three quadrotors along the spiral path has been magnificently performed.

Moreover, in the second one, the three quadrotors linearly touch the s-shaped path. In this case, both the geometric shape of the quadrotors and the desired path have been changed compared to the previous mission. The simulation results for the second mission are shown in Figures 37 through 39. Figures 37 and 38 represent the position and attitude of three quadrotors, respectively. Figure 39 shows the 3-D scheme of three quadrotors. These simulation results show that the followers have tracked the leader and the formation has been entirely performed.

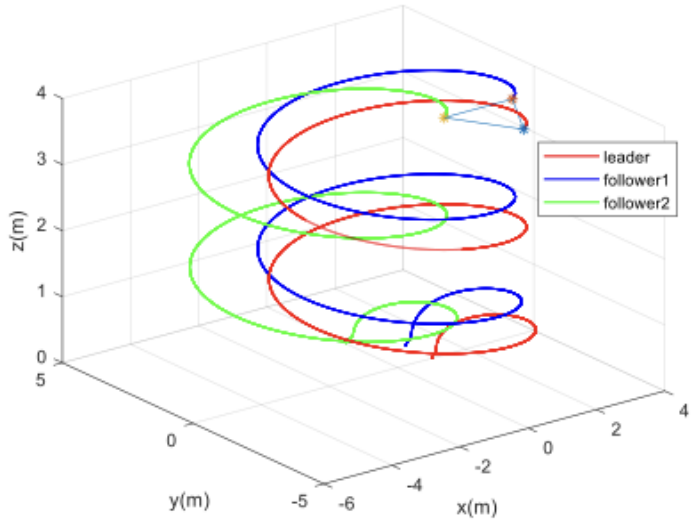

Figure 36: Three-dimensional diagram of three quadrotors along the spiral path

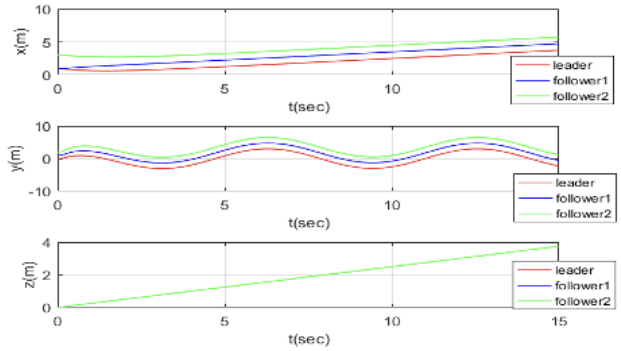

Figure 37: Response of position of three quadrotors along the s-shaped path

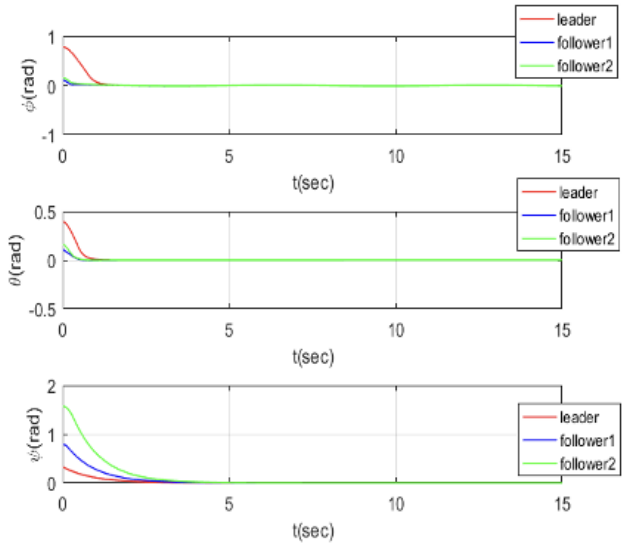

Figure 38: Response of attitude of three quadrotors along the s-shaped path

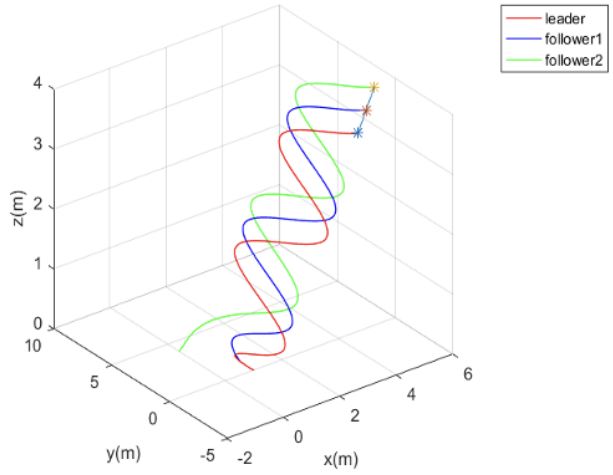

Figure 39: Three-dimensional diagram of three quadrotors along the s-shaped path

The third mission is the same as the previous mission, with a different number of followers. These simulation results show in figures 40 through 42. Figures 40 and 41 represent the position and attitude of five quadrotors, respectively. Figure 42 shows the three-dimensional plan for five quadrotors. These simulation results show that an increasing number of quadrotors can do the formation task successfully.

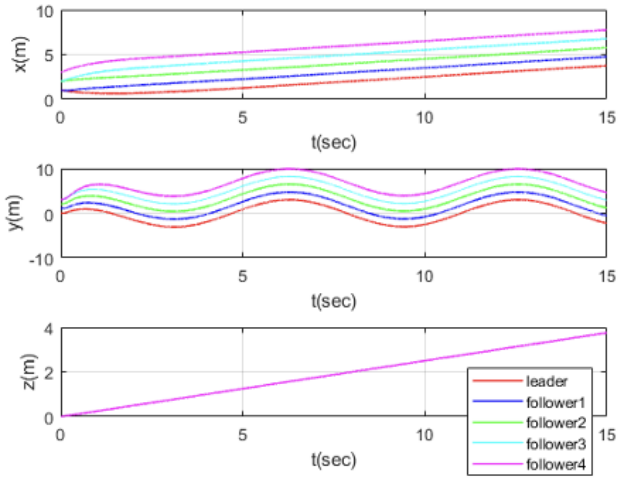

Figure 40: Response of position of five quadrotors along the s-shaped path

The results of these three missions with different paths, different geometry, and the different number of agents indicate that the formation succeeds properly.

8 Conclusion

Sliding mode leader-follower formation strategies for multi-quadrotors are discussed in the present study. A comparison of the suggested simulation results shows that the terminal-sliding mode has less convergence time than the classic SMC does. It decreases in super-twisting but this controller has unwished overshoot. In the nonsingular terminal super twisting SMC, the convergence time was approximately 5% less than that of the super-twisting ones, and the outputs tracked the reference without any chattering and overshooting. Due to the better results, the nonsingular terminal super-twisting sliding mode controller was applied to control the position and attitude of the plants in flight

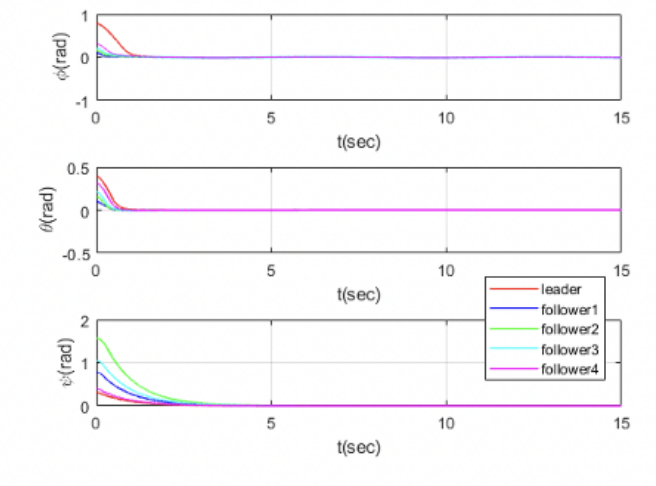

Figure 41: Response of attitude of five quadrotors along the s-shaped path

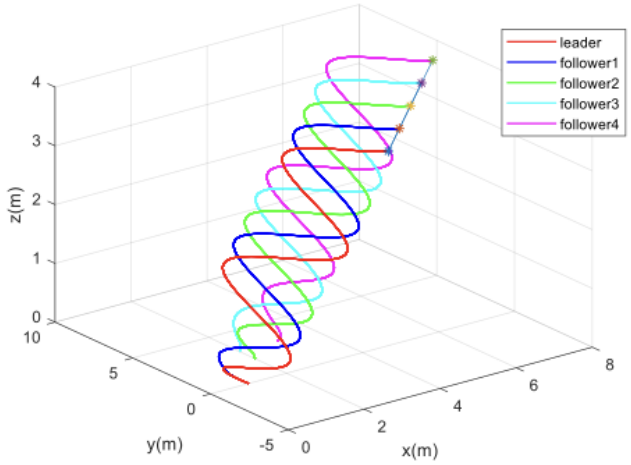

Figure 42: Three-dimensional diagram of five quadrotors along the s-shaped path

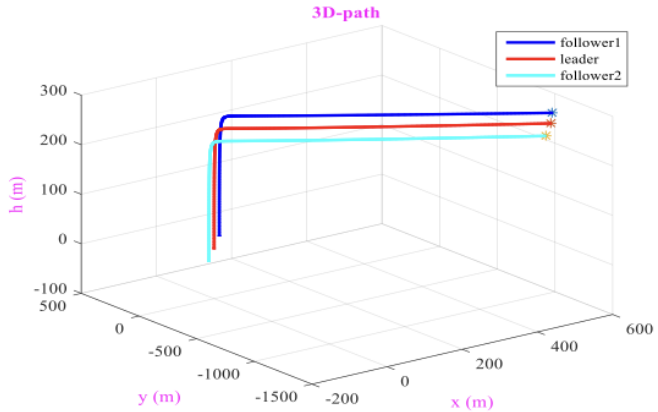

Figure 43: Three-dimensional diagram of three quadrotors along the linear path

formation. The simulation results for three missions with different numbers of agents and dissimilar paths correspond-

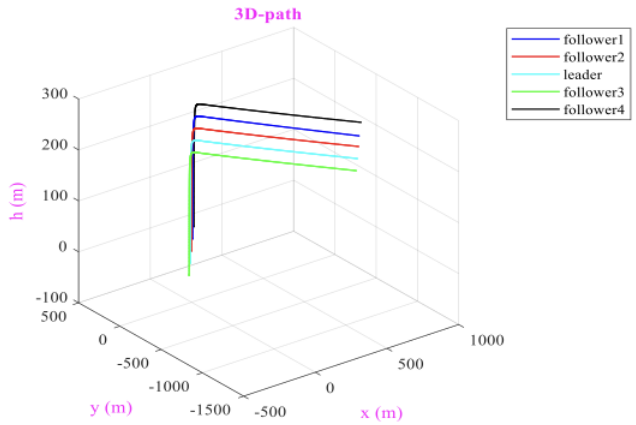

Figure 44: Three-dimensional diagram of five quadrotors along the linear path

ingly indicate that the formation does properly. The robust formation for MAS with obstacle avoidance and preserve connectivity can be considered in the future studies of the authors.

References

[1] A. Abdessameud, A. Tayebi, and I. G. Polushin, *Motion coordination of thrust-propelled underactuated vehicles in the presence of communication delays*, 19th IFAC Cong., 2014, pp. 3170–3175.

[2] R. Adderson and Y. J. Pan, *Terminal sliding mode control for the formation of a team of quadrotors and mobile robots*, IECON 47th Ann. Conf. IEEE Ind. Electron. Soc., 2021, pp. 1–6.

[3] I. Bayezit and B. Fidan, *Distributed cohesive motion control of flight vehicle formations*, IEEE Trans. Ind. Electron. **60** (2013), no. 12, 5763–5772.

[4] A. Bemporad and C. Rocchi, *Decentralized hybrid model predictive control of a formation of unmanned aerial vehicles*, 18th IFAC World Cong. **44** (2011), no. 1, 11900–11906.

[5] H. Cai and J. Huang, *The leader-following consensus of multiple rigid spacecraft systems*, Amer. Control Conf. ACC **13** (2013), 824–829.

[6] T. Dierks and S. Jagannathan, *Neural network control of quadrotor UAV formations*, Amer. Control Conf. ACC. **9** (2009), 2990–2996.

[7] F. Gao and Y. Jia, *Distributed finite-time coordination control for 6dof spacecraft formation using nonsingular terminal sliding mode*, Proc. 2015 Chinese Intell. Syst. Conf., 2016, pp. 195–204.

[8] H. Ghadiri, M. Emami, and H. Khodadadi, *Adaptive super-twisting non-singular terminal sliding mode control for tracking of quadrotor with bounded disturbances*, Aerospace Sci. Technol. **112** (2021), 106616.

[9] J. González-Sierra, A. Dzul, and E. Martínez, *Formation control of distance and orientation based-model of an omnidirectional robot and a quadrotor UAV*, Robotics Auton. Syst. **147** (2022), 103921.

[10] Z. Hou, X. Yu, and P. Lu, *Terminal sliding mode control for quadrotors with chattering reduction and disturbances estimator: Theory and application*, J. Intell. Robotic Syst. **105** (2022), no. 4, 1–21.

[11] S. Islam, P. X. Liu, and A. E. Saddik, *Robust control of four rotor unmanned aerial vehicle with disturbance uncertainty*, IEEE Trans. Ind. Electron. **62** (2015), no. 3, 1563–1571.

[12] A. Karimoddini, M. Karimadini, and H. Lin, *Decentralized hybrid formation control of unmanned aerial vehicles*, arXiv preprint arXiv:1403.0258 (2014), 3887–3892.

[13] M. Labbadi, M. Djemai, and S. Boubaker, *A novel non-singular terminal sliding mode control combined with integral sliding surface for perturbed quadrotor*, Proc. Inst. Mech. Engin., Part I: J. Syst. Control Engine. **236** (2022), no. 5, 999–1009.

[14] M. Labbadi, K. Elyaalaoui, M. Dabachi, S. Lakrit, M. Djemai, and M. Cherkaoui, *Robust flight control for a quadrotor under external disturbances based on predefined-time terminal sliding mode manifold*, J. Vibr. Control **29** (2022), no. 9-10, 2064–2076.

[15] P. Manouchehri, R. Ghasemi, and A. Toloei, *Distributed fuzzy adaptive sliding mode formation for nonlinear multi-quadrotor systems*, Int. J. Engin. **33** (2020), no. 5, 798–804.

[16] A.J. Marasco, S.N. Givigi, M. Iskandarani, S. Yousefi, and C.A. Rabbath, *Solving multi-UAV dynamic encirclement via model predictive control*, IEEE Trans. Control Syst. Technol. **23** (2015), no. 6, 2251–2265.

[17] O. Mechali, J. Iqbal, A. Mechali, X. Xie, and L. Xu, *Finite-time attitude control of uncertain quadrotor aircraft via continuous terminal sliding-mode-based active anti-disturbance approach*, IEEE Int. Conf. Mechatron. Autom., 2021, pp. 1170–1175.

[18] O. Mechali, L. Xu, Y. Huang, M. Shi, and X. Xie, *Observer-based fixed-time continuous nonsingular terminal sliding mode control of quadrotor aircraft under uncertainties and disturbances for robust trajectory tracking: Theory and experiment*, Control Engin. Practice **111** (2021), 104806.

[19] N.P. Nguyen, D. Park, D.N. Ngoc, N. Xuan-Mung, T.T. Huynh, T.N. Nguyen, and S.K. Hong, *Quadrotor formation control via terminal sliding mode approach: Theory and experiment results*, Drones **6** (2022), no. 7, 172.

[20] U. Pilz, A. Popov, and H. Werner, *Robust controller design for formation flight of quad-rotor helicopters*, Joint 48th IEEE Conf. Decis. Control 28th Chinese Control Conf., 2009, pp. 8322–8327.

[21] G. Regula and B. Lantos, *Formation control of quadrotor helicopters with guaranteed collision avoidance via safe path*, Electric. Engin. Comput. Sci. **4** (2012), no. 56, 113–124.

[22] M. Saska, Z. Kasl, and L. Preucil, *Motion planning and control of formations of micro aerial vehicles*, 19th IFAC Congress **47** (2014), no. 3, 1228–1233.

[23] M. Turpin, N. Michael, and V. Kumar, *Decentralized formation control with variable shapes for aerial robots*, IEEE Int. Conf. Robotics Autom., 2012, pp. 23–30.

[24] M. Turpin, N. Michael, and V. Kumar, *Trajectory design and control for aggressive formation flight with quadrotors*, Auton. Robots **33** (2012), no. 1-2, 143–156.

[25] M. Turpin, N. Michael, and V. Kumar, *Capt: Concurrent assignment and planning of trajectories for multiple robots*, Int. J. Robotics Res. **33** (2014), no. 1, 98–112.

[26] S. Yang, J. Mao, and F. Xu, *Integral terminal sliding mode control for quadrotor based on a novel power reaching law*, Int. Conf. Comput. Control Ind. Engin., 2022, pp. 177–192.